An Open Gate for High-Density Metal Ions in N-doped Carbon Networks: Powering Fe-N-C Catalyst Efficiency in Oxygen Reduction Reaction

Journal:	*ACS Catalysis*
Manuscript ID	cs-2021-01638s.R1
Manuscript Type:	Article
Date Submitted by the Author:	n/a
Complete List of Authors:	Zhang, Xiong; Universite de Strasbourg, Institut de Chimie et des Procedes pour l'Energie, l'Environnement et la Sante (ICPEES), ECPM, CNRS Truong-Phuoc, Lai; Universite de Strasbourg, Institut de Chimie et des Procedes pour l'Energie, l'Environnement et la Sante (ICPEES), ECPM, CNRS Liao, Xuemei; Sichuan University, Chemimal Engineering Tuci, Giulia; Istituto di Chimica dei Composti Organo Metallici Consiglio Nazionale Delle Ricerche Sezione di Firenze, Fonda, Emiliano; Synchrotron SOLEIL Papaefthimiou, Vasiliki; LMSPC-UMR 7515 du CNRS, Zafeiratos, Spyridon; CNRS-UDS, aLaboratoire des Matériaux, Surfaces et Procédés pour la Catalyse (LMSPC) Giambastiani, Giuliano; National Research Council, Institute of Chemistry of OrganoMetallic Compounds Pronkin, Sergey; Universite de Strasbourg, Institut de Chimie et des Procedes pour l'Energie, l'Environnement et la Sante (ICPEES), ECPM, CNRS Pham-Huu, Cuong; Universite de Strasbourg, Laboratoire des Matériaux, Surfaces et Procédés pour la Catalyse

An Open Gate for High-Density Metal Ions in N-doped Carbon Networks: Powering Fe-N-C Catalyst Efficiency in Oxygen Reduction Reaction

Xiong Zhang,[δ] *Lai Truong-Phuoc,*[δ] *Xuemei Liao,* [δ,φ] *Giulia Tuci,*[ω] *Emiliano Fonda,*[ξ] *Vasiliki Papaefthymiou,*[δ] *Spyridon Zafeiratos,*[δ] *Giuliano Giambastiani,*[δ,ω,]* *Sergey Pronkin,*[δ,]*
Cuong Pham-Huu [δ,]*

[δ] *Institute of Chemistry and Processes for Energy, Environment and Health (ICPEES), ECPM, UMR 7515 CNRS-University of Strasbourg, 25 rue Becquerel, 67087 Strasbourg Cedex 02, France.* giambastiani@unistra.fr, sergey.pronkin@unistra.fr, cuong.pham-huu@unistra.fr

[φ] *School of Food and Biological Engineering, Xihua University, 610039, Chengdu, China*

[ω] *Institute of Chemistry of OrganoMetallic Compounds, ICCOM-CNR and Consorzio INSTM, Via Madonna del Piano, 10 – 50019, Sesto F.no, Florence, Italy.* giuliano.giambastiani@iccom.cnr.it

[ξ] *Synchrotron SOLEIL, L'Orme des Merisiers Saint-Aubin BP 48 91192 Gif-sur-Yvette Cedex, France.*

Abstract

Non-noble metal catalysts for the oxygen reduction reaction (ORR) showing catalytic activity comparable or even superior to that of the benchmark Pt/C are highly attractive systems for the development of a mature fuel cells technology. Fe-N-C moieties exhibit excellent performance in the oxygen reduction reaction (ORR) although a synthetic strategy for their production still remains a challenging matter of catalysis and material science. Herein, an original and general protocol for the preparation of high-density and discrete Fe-N-C-based single-atom catalysts has been proposed starting from cheap and food-grade raw components. The rational combination of chelating citrate ions with the ancillary monodentate $^{-}$SCN ligand has established as an “open gate” for water soluble iron ions to be accommodated in the form of Fe-N-C moieties within final C-N networks. Although recent findings in the field of electrocatalysis have pointed out the often-beneficial synergistic action between isolated and metallic iron species or iron carbides and their protecting C-N shells, the poor selectivity on the nature of the final Fe-species in N-doped C-networks remains matter of debate and does not contribute to shed light on the effective nature of the active species in the process. The highly metal-loaded catalysts in the form of highly dispersed Fe-N-C moieties prepared with the synthetic protocol described in the paper have been tested as electrocatalysts in the oxygen reduction reaction (ORR), showing electrocatalytic performance under alkaline environment that rank among the highest reported so far for related Fe single atom catalysts (Fe-SACs) of the *state-of-the-art*.

KEYWORDS: Non-precious metal catalysts; Electrocatalysis; Oxygen reduction reaction; Fe-N-C catalysts, iron oxyhydroxide networks

Introduction

Reduce the utilization of fossil fuels and improve the conversion efficiency of clean and renewable energy sources is becoming an urgent priority of modern chemistry and chemical engineering. Addressing this goal is a crucial issue not only related to the steadily fossil fuel depletion but also to face with all main environmental and climate concerns caused by their massive use. Fuel cell technology is receiving great deal of interest in the exploration of sustainable energy systems because it allows to join zero-carbon emissions with high energy conversion efficiency in the same device.[1] In spite of that, the exploitation of fuel cell devices is hurdled by high cost of its components, particularly of noble metal-based electrode materials. Loadings as high as 0.4 mg cm^{-2} of platinum are generally required at the fuel cell cathode for promoting the kinetically sluggish oxygen reduction reaction.[2] Therefore, the synthesis of low-cost advanced materials with improved catalytic performance and high robustness, employing non-critical components is becoming a challenging research topic with great expectations for the next-generation energy devices.

For more widely used H_2-O_2 fuel cells (PEMFC, AFC), the kinetically sluggish oxygen reduction process (ORR) falls among the most investigated reactions with both metal-[3] and metal-free[4-5] catalysts.[6] On this regard, the last years have witnessed impressive progresses in the development of innovative synthetic methodologies for the straightforward preparation of efficient (electro)catalysts from cheap and non-critical components with a special attention to the replacement of scarce and costly platinum-group metals (PGMs).[7-8] In addition, researchers have committed in controlling the shape and reducing the size of catalysts active phases from a nanometer scale down to few-atoms cluster-sized metals up to single atomic site catalysts (SACs). Such an effort has been dictated by the need of reducing the active-phase amount, maximizing the atom utilization and optimizing the metals microenvironment by improving their stabilization with appropriate donor atom sets. In other words, all this work has been focused on the improvement of catalysts performance in key (electro)catalytic processes.[9-13] Although reducing nanocatalysts sizes down to atomically dispersed metal systems still represents a challenging matter,[14] it is commonly recognized that controlling electronic and geometric structural features of metal exposed sites is the key tool to get catalysts exhibiting unique performance.[15-17]

Some of us have recently proposed a green and versatile synthetic technology for the preparation of N-enriched mesoporous carbon-based materials starting from cheap and food-grade raw building blocks.[18-20] Such an approach was successfully used to get from powders to hierarchically organized 3D foam structures[18-19] and organic-inorganic composites[21-23] to be employed as effective, stable and single-phase metal-free systems for catalyzing a relatively wide number of industrially relevant transformations. At odds with more conventional methods to produce N-rich carbon networks, *i.e.* the chemical-vapor-deposition (CVD) technique, C and N sources employed for the synthesis of these novel materials were selected from commonly available solid feedstocks to be simply dissolved in water. D-glucose ($C_6H_{12}O_6$) was selected as C-source, a leavening agent [*i.e.* ammonium carbonate $(NH_4)_2CO_3$)] as N-source and citric acid ($C_6H_8O_7$) as a sacrificial carrier for harvesting and conveying NH_3 released from the carbonate decomposition under the form of ammonium citrate [$HO\text{-}C_3H_4(COO)_3H_x(NH_4)_{3-x}$)] (x = 0-3). Successive and controlled material thermal treatments have led to mesoporous carbon networks featuring with relatively high specific surface areas (*i.e.* 150 m^2 g^{-1}) and N-contents up to 5 wt.%.

The presence of a potentially tridentate chelating agent (*i.e.* citrate ions) prompted us to reconsider our original metal-free scheme as a protocol for the preparation of highly dispersed and atomically sized metal-based catalysts. Indeed, citrates are known to act as chelating agents towards a variety of transition metals, forming relatively stable and water-soluble complexes. Accordingly, their generation can be regarded as an “open gate” for water soluble metal ions to be accommodated within final C-N networks.

Although in the past few years’ huge efforts have been devoted to power single-atom catalysts technology within light-heterodoped nanocarbon networks, their large-scale production with a high metal-active site density, avoiding the generation of inhomogeneous metal agglomerates or the co-generation of less active metal species, remains a challenging task to be properly addressed.

Seminal works from two independent teams have recently shed light on the role of thiocyanate ($^{-}$SCN) as a sacrificial ancillary ligand for Fe-metal ions in the synthesis of atomically dispersed Fe-N-C composites with superior electrocatalytic activity.[24-25] In particular, Chu, W. and Wu, C. have demonstrated the role of sulfur ligands addition (in the form of $^{-}$SCN) to a mixture of 2,2-bipyridine and $FeCl_3$ on the ultimate composition of an acid-washed CNT-coating layer obtained from the materials pyrolysis at 900 °C.[24] They found that S-salt addition to the mixture during pyrolysis resulted in the formation of Fe-sulfides mainly instead of the more acid-resistant Fe carbides. Given the higher solubility of the former in acidic media, the large excess of Fe not present in the form of Fe-N_x coordinated ions was easily etched and removed during the washing treatment, leaving behind atomically dispersed Fe-N_x species.[26] Wei, Z. and co-workers proposed another intriguing example for the control of SACs in Co-N/C systems through the pyrolysis of an urea and glucose mixture in the presence of $^{-}$SCN as the counterion for a Co^{2+} salt precursor.[27] They found that $^{-}$SCN addition reduced the temperature at which Co-rich particles grew respect to the temperature at which their C-shell encapsulation occurred. Accordingly, their removal along with other various impurities was easily accomplished by a simple acid washing while preserving the SACo-N/C active phases only.

Herein, we put forward a novel and effective approach towards the preparation of highly dispersed Fe-N-C frameworks starting from the chelating ability of the potentially tridentate citrate ion towards an Fe^{3+} salt as metal precursor. The simultaneous entering of the monodentate thiocyanate (^{-}SCN) ion in the metal coordination sphere was found highly beneficial for the ultimate preparation of a Fe-N-C composite. Indeed, the excess of iron not stabilized in the form of Fe-N-C nuclei throughout the high-temperature pyrolysis, was preferably converted into iron sulfide species easier to be etched and removed than iron carbides upon the sample acid washing. Although any mechanistic consideration on the Fe-coordinated ^{-}SCN ion(s) during the material pyrolysis remains merely speculative, our outcomes leave no doubts that catalysts prepared without the addition of ^{-}SCN ions originate more inhomogeneous Fe-containing samples with the evident formation of iron-carbide nanoparticles to a markedly higher extent. The as-prepared Fe-N-C catalysts (with and without ^{-}SCN) have been thoroughly characterized and scrutinized in turn as ORR electrocatalysts under alkaline environment. Noteworthy, Fe/NSC^{N} (**1^{N}**) has shown excellent electrocatalytic performance ranking among the most effective Fe-based SACs presented in this contribution as well as compared to related Fe-SACs reported so far in the literature for a $4e^{-}$ reduction process under alkaline environment.

Results and discussion

We described a modification of a proprietary protocol already applied to the preparation of N-enrich C-networks starting from cheap and food-grade components.[20] At odds with our previous reports on the preparation of N-doped carbons to be applied as metal-free catalysts for a variety of challenging and industrially-relevant transformations,[18-19, 22] the synthetic scheme reported hereafter aims at obtaining iron-doped networks to be employed as catalytically active samples in a challenging electrochemical process. To this aim, D-glucose, citric acid and $(NH_4)_2CO_3$ were combined with a proper amount of KSCN (potassium thiocyanate) and the solid mixture was dissolved in 25 mL of ultrapure water. After an initial effervescence due to CO_2 evolution, a mixed ammonium/potassium citrates yellow-orange solution was formed. Its subsequent treatment with a water solution of $FeCl_3 \cdot 6H_2O$ (iron trichloride hexahydrate) showed the appearance of a blood-red color likely due to the transient generation of $[Fe(SCN)_n(H_2O)_{6-n}]^{(3-n)+}$ (n = 1-3) aquo complexes,[28] that quickly turned to orange-yellow. Such a rapid color change was attributed to the competitive coordination between the monodentate thiocyanate ion and the potentially tripodal citrates. The resulting mixture was thought to generate an extensive ionic network that gave rise to a hygroscopic brownish gel (Fe/NSC^g, **1**^{g}) after slow solvent evaporation in an oven at 110 °C overnight (Figure 1). **1**^{g} was then pyrolyzed at 900 °C under Ar atmosphere for 1 h during which highly dispersed Fe-N-C sites within an extensively graphitized carbon network and iron-based particles were formed (Fe/NSC^p, **1**^{p}). The as obtained sample was then leached in a diluted H_2SO_4 solution at 80 °C for 8h to give **1**^{w} (Fe/NSC^w). Such an acid treatment was used to remove the excess of unreactive iron-containing species formed during the pyrolysis step (*vide infra*).[24-25, 27] The use of KSCN in the mixture was intended to positively contribute to the generation of a sample containing dispersed Fe-N-C sites. Indeed, the presence of coordinating sulfur ions in the donor atoms set has already shown to foster the conversion of excess of iron not stabilized in the form of Fe-N-C moieties into Fe-sulfides.[24] As a matter of fact, the generation of more acid-resistant and potentially carbon-coated Fe or Fe_3C particles was deeply inhibited while Fe-S_x species were conveniently leached out upon the acid material treatment.[26]

As a proof of concept, the same synthetic procedure was reproduced without the use of KSCN in the starting mixture as to afford Fe/NC^g (**2**^{g}), Fe/NC^p (**2**^{p}) and Fe/NC^w (**2**^{w}) counterparts. Figure

2 outlines selected but representative features of the two materials at comparison. Both pyrolyzed samples (**1**^{p} and **2**^{p}) contained distinctive XRD diffraction peaks due to the presence of iron particles. Peaks at 2θ values of ≈ 43 °, ascribed to the presence of iron carbide (Fe_3C)[29-31] species were present on both samples.

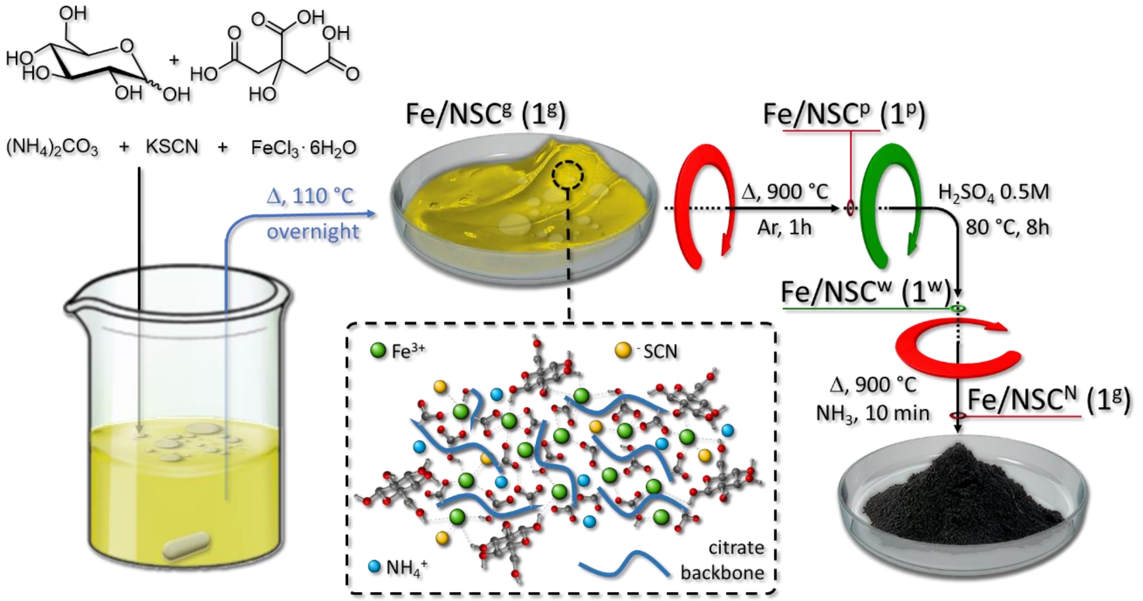

Figure 1. Step-by-step synthetic procedure for the preparation of atomically dispersed Fe-N-C sites form cheap and food-grade C/N precursors.

Anyhow, it is clear how their intensity on the sample prepared with KSCN (**1**^{p}) was markedly lower compared to **2**^{p} (Figure 2A). Moreover, distinctive reflection peaks at 2θ = 28.4, 30.4 and 32.2 ° present in Fe/NSC^p (**1**^{p}) only were attributed to the generation of iron sulfide species.[32-33] Noteworthy, the acid washing of the two samples with diluted H_2SO_4 resulted in the complete removal of iron and iron sulfide particles from **1**^{p} while few crystalline phases associated with Fe_3C and Fe species more acid-resistant or encapsulated in the C-networks were still present in **2**^{w} (Figure 2A *vs*. 2B).

From a qualitative viewpoint, the XRD profiles of the two acid washed samples account for C-based materials featuring with differently sized crystallites,[34] with the smallest ones being those obtained from the KSCN-containing mixture. From a morphological view-point, the two samples presented close specific surface areas and pore-size distribution (see Table 1).

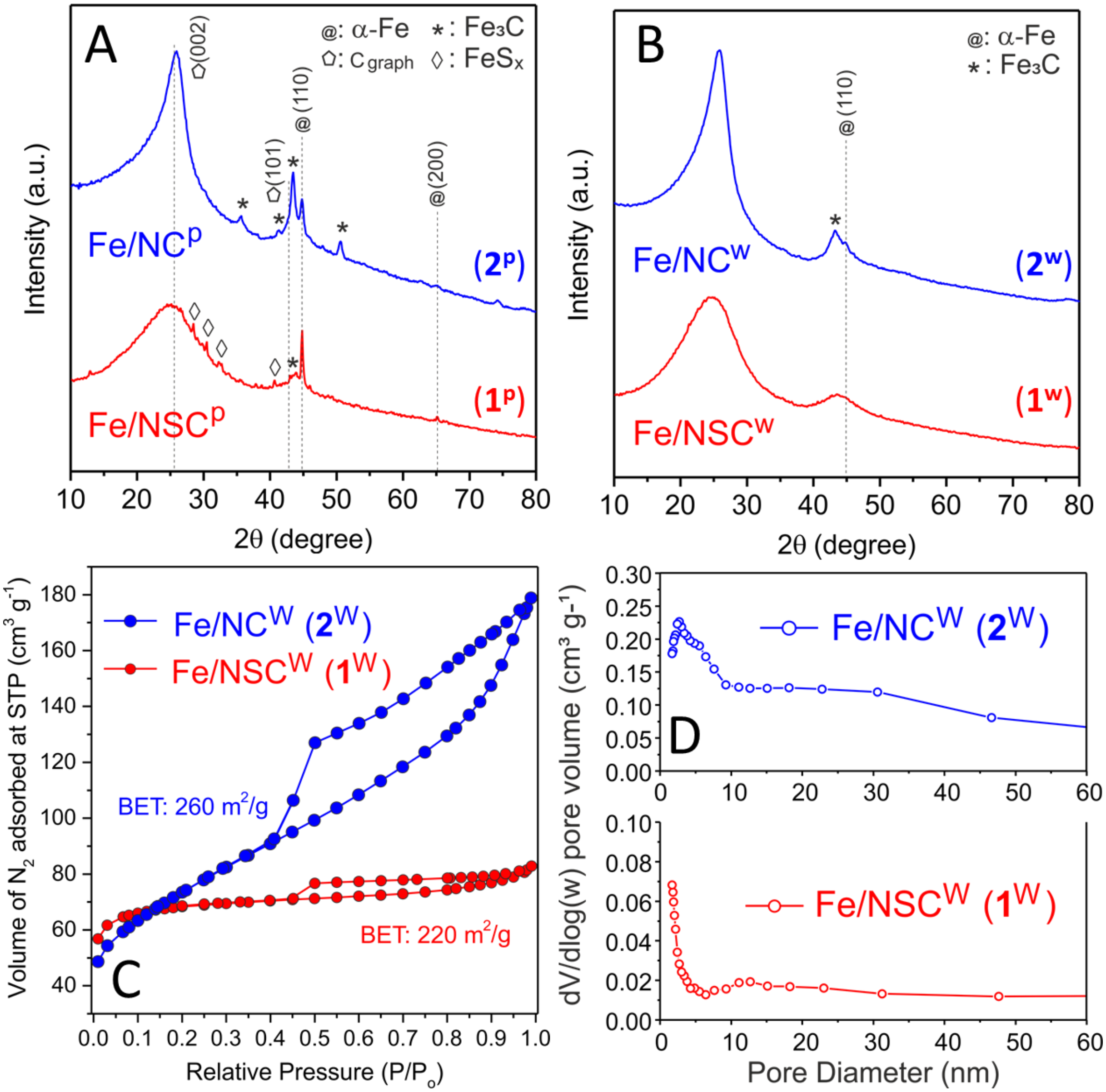

Figure 2. XRD profiles of Fe/NSC^X (**1**^{X}) and Fe/NC^X (**2**^{X}) before (x = **p**; A) and after (x = **w**; B) acid treatment with a 0.5 M H_2SO_4 solution at 80 °C for 8h. (C) N_2 adsorption-desorption isotherm linear plot of Fe/NSC^w (**1**^{w}) (red curve) and Fe/NC^w (**2**^{w}) samples (blue curve) recorded at 77 K along with (D) the respective pore-size distributions (BJH method) based on the adsorption branch.

As Figures 2C-D show, regardless the use of KSCN in the mixture, samples presented type IV isothermal profiles with distinctive H2 hysteresis loops in the 0.45-1.0 P/P_0 range, typical of mesoporous networks featured by complex pore structures of ill-defined shape.[35] Sample Fe/NC^{w} (**2**^{w}) showed a more pronounced hysteresis loop associated to the presence of a large extent of mesopores (Figure 2D) that facilitated the occurrence of capillary condensation phenomena.

Afterwards, **1**^{w} and **2**^{w} underwent an additional thermal treatment at 900 °C for 10 min in the presence of ammonia (Figure 1 and Experimental Section). Such a thermo-chemical phase is known to produce beneficial effects on Fe-doped carbon-based structures, especially N-enriched ones, to be employed as ORR electrocatalysts.[36] Indeed, the corrosive action of the NH_3 treatment combined with high operative temperatures, changes the morphology of the iron-hosting networks by increasing their surface areas and micropore density (Table 1).[37-40] At the same time, NH_3 treatment was known to foster the generation of more active iron-based electrocatalysts by increasing the surface density of Fe-N_x species engaged in ORR.[38] As expected, a significant increase of specific surface areas was measured on both samples and in particular on **1**^{N} whose SSA value and total pore volume grew up to three times that of its acid washed precursor **1**^{w} (Table 1 and Figure 3A,B).

XPS analysis and elemental analysis on both samples before and after annealing with ammonia were used to verify the effect of the thermo-chemical treatment on the total N-contents and N-composition of the as-prepared samples. As Figure S1 shows, all materials presented almost superimposable survey profiles featured by the same distinctive peaks whose relative percentages were used to semi-quantitatively fix the N-content on each sample (Table 1). Although the metal contents in **1**^{N} and **2**^{N} has been determined by inductively coupled plasma (ICP) analyses (Table 1) and the NH_3 treatment was supposed to have negligible or no effects on its ultimate % in the samples, it is worthy to note that XPS survey spectra of both NH_3-annealed materials (**1**^{N}-**2**^{N}) show the presence of distinct Fe peaks not visible in the simply washed samples (**1^w-2^w**). This result was ascribed to the joint corrosive/doping action of NH_3 during the last annealing phase. Indeed, it was expected to increase the surface exposure of catalytically active Fe-N sites.

Elemental analysis (EA, Table 1) was finally employed to better quantify the N-content before and after materials NH_3-annealing. According to XPS analyses and irrespective to the general decrease of the samples weight after the last thermal treatment (roughly measured in about 25-35 wt.% loss passing from **1^w-2^w** to **1^N-2^N** samples), N-content in **1^N** and **2^N** increases upon NH_3-annealing (Table 1). These data have been finally confirmed by EA (Table 1). Deconvolution of high-resolution spectra at their N 1s core regions accounted for five distinct N-components whose relative % (before and after the thermo-chemical treatment) were used to fix the materials composition (Table 1, Figure 3C and Figure S2). Although the increase of N-content in the ammonia treated samples makes questionable to comment on the specific modification of relative N% of these samples passing from **1^w-2^w** to **1^N-2^N**, Figures S2 clearly unveil an appreciable increase of the components at 399.9 eV in **1^N-2^N**, conventionally ascribed to iron-coordinated N sites (Fe-N).[41-42] This evidence has confirmed the role of the NH_3 treatment with respect to the increase of Fe-N_x surface density.[38] Lastly, the NH_3-annealing operated under severe conditions (see experimental section) was found to deeply and positively affect the catalytic properties of the final composites (*vide infra*).[36] As discussed earlier in brief, this thermo-chemical phase increased the specific surface areas and the material total pore volume appreciably through an etching action on the carbon carrier (Table 1).[43] At the same time the overall N-content increased (Table 1) thus making the NH_3 etching/doping action[38] a key tool for the generation of more porous and N-basic enriched[44] networks containing surface exposed Fe-N-C moieties as accessible sites for the catalytic process to occur.[45]

As far as the Fe content and particles distribution in the two acid-leached and NH_3-annealed samples is concerned, the material prepared with $^{-}$SCN (**1**$^{\mathrm{N}}$) did not show any obvious metal cluster or metal-aggregate formation (*vide infra*) in spite of a Fe loading higher (> 35 wt.%) than that measured on the $^{-}$SCN-free counterpart (**2**$^{\mathrm{N}}$).

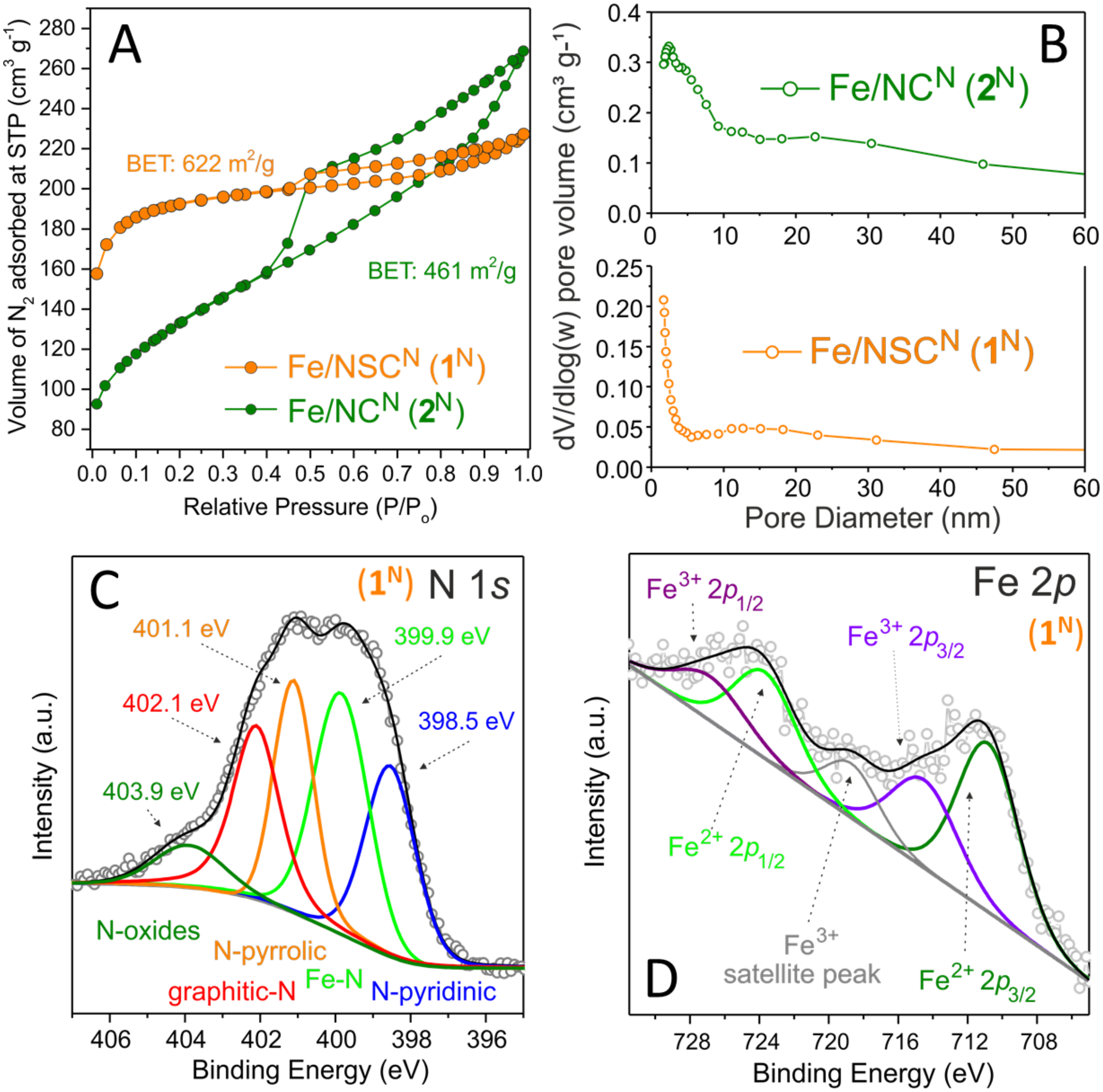

Figure 3. (A) N_2 adsorption-desorption isotherm linear plot of Fe/NSC$^{\mathrm{N}}$ (**1**$^{\mathrm{N}}$) (orange curve) and Fe/NC$^{\mathrm{N}}$ (**2**$^{\mathrm{N}}$) (green curve) samples recorded at 77 K along with (B) the respective pore-size distributions (BJH method) based on the adsorption branch. XPS spectra of high-resolution N 1s (C) and Fe 2p (D) core regions of Fe/NSC$^{\mathrm{N}}$ (**1**$^{\mathrm{N}}$).

High-resolution transmission electron microscopy (TEM) has unambiguously provided a clear-cut difference in terms of composition of the two samples at comparison (**1**^{N} *vs*. **2**^{N}). While **2**^{N} revealed the presence of a certain number of nanoparticles (Figure S3A-B) with a relatively narrow size distribution (10 nm as mean NPs ∅ size), high-resolution images at the different magnifications carried out on **1**^{N} were consistent with relatively well graphitized carbon networks containing only rare iron clusters randomly distributed all over the sample (Figures 4A-D and Figure S3C-D). A more careful analysis of these acid-resistant clusters on both materials has been used to unveil their nature. Figure S3B refers to the high magnification image recorded on an iron cluster of **2**^{N} and it shows the presence of a crystalline phase with a distinctive interplanar distance of 0.21 nm, characteristic of (211) planes of a Fe_3C phase.[31, 46-47]

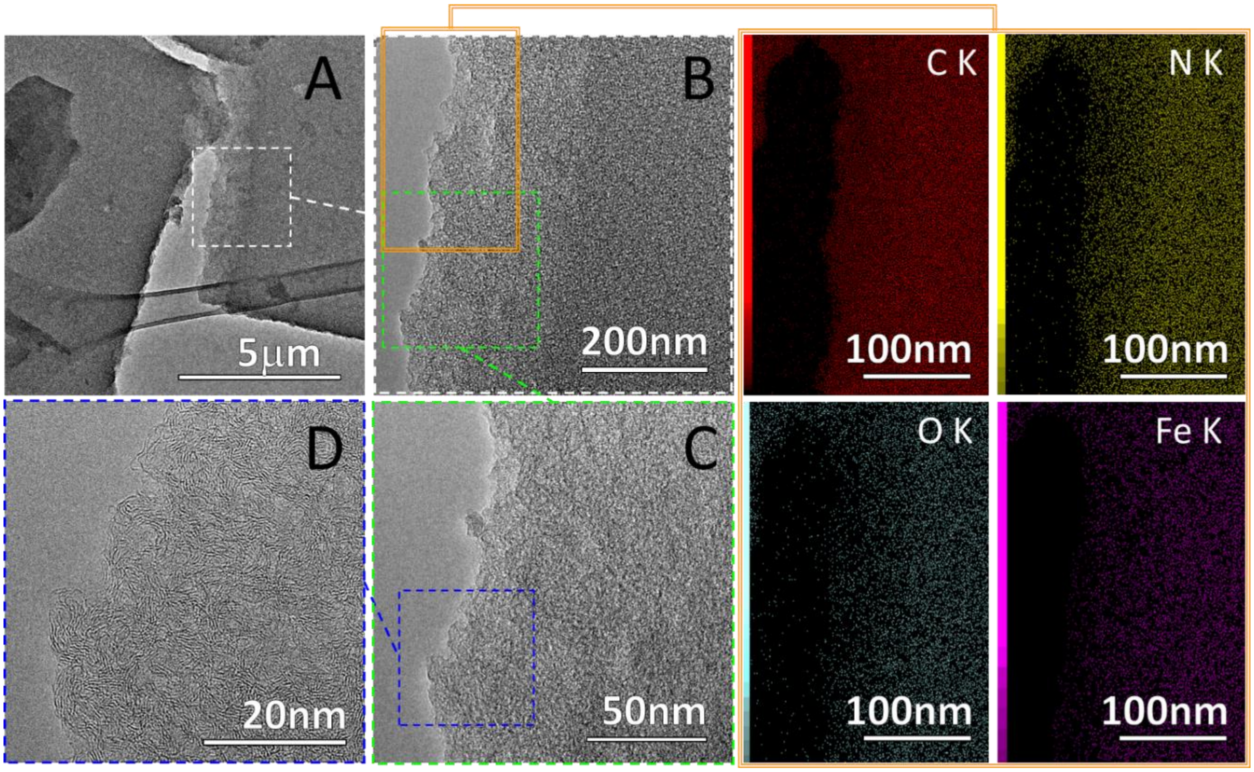

Figure 4. Representative HR-TEM images at different magnifications of **1**^{N} (A-D) along with EDX elemental composition on a selected region of the sample. Images at various magnifications demonstrate the virtual absence of large metal aggregates all over the sample. EDX mapping unveils the atomically dispersion nature of Fe sites all over the scanned area.

Equally, rare metal aggregates on **1**$^{\mathbf{N}}$ (Figure S3C-D) have shown the same crystalline phase and thus the same composition of these residual iron clusters. At odds with a virtually iron-clusters-free nature of **1**$^{\mathbf{N}}$, the energy-dispersive X-ray (EDX) mapping carried out on this sample (Figure 4, right side hand images) has shown a homogeneous distribution/doping of dispersed Fe nuclei along with N and O elements throughout the whole carbon network.

Electron microscopy and EDX analysis support the evidence of remaining iron species in **1**$^{\mathbf{N}}$ under the form of highly dispersed nuclei confined and stabilized within the graphitized carbon layers. Traces of sulfur seem still present in this sample (Figure S4) although the acid washing first, and the NH_3-thermal annealing later were supposed to eliminate it almost completely. Indeed, part of sulfur was leached away under the form of Fe-based sulfides upon the sample acid washing, part was then thermally decomposed during the annealing step where the thiocyanate was converted into cyanide and elemental sulfur[48] with the latter being transformed into H_2S and N_2 upon reaction with NH_3 at high temperature.[49]

Table 1. Selected chemico-physical and morphological properties of catalysts and precursors

Entry	Sample	SSA^{a} (m^{2} g^{-1})	Total pore volume (cm^{3} g^{-1})^{b}	t-plot micropore volume (cm^{3} g^{-1})^{c}	Fe wt.%^{d}	Fe at.%^{e}	N wt.% (from EA)	XPS data, N-species (%)^{f}					
								N at.%^{e}	Pyridinic	Fe-N	Pyrrolic	Graphitic	Oxidized
1	Fe/NSC^{w} (**1**$^{\mathbf{w}}$)	220	0.125	0.084	n.d.	n.d.	5.4	3.7	21.8	25.9	30.3	17.4	4.6
2	Fe/NSC^{N} (**1**$^{\mathbf{N}}$)	622	0.346	0.235	2.54	1.7	6.0	6.1	21.9	31.1	19.8	20.8	6.4
3	Fe/NC^{w} (**2**$^{\mathbf{w}}$)	260	0.268	0.015	n.d.	n.d.	5.2	4.3	26.7	23.3	29.9	17.9	2.2
4	Fe/NC^{N} (**2**$^{\mathbf{N}}$)	461	0.406	0.058	1.67	0.9	5.7	4.6	26.8	25.4	20.1	20.5	7.2
5	NSC^{N} (**3**$^{\mathbf{N}}$)	618	0.318	0.251	-	-	6.8	6.8	51.4	-	36.5	9.3	2.9

[a] Brunauer-Emmett-Teller (BET) specific surface area (SSA) measured at T = 77 K. [b] Total pore volume determined using the adsorption branch of N_2 isotherm at $P/P_0 = 0.98$. [c] Determined by t-plot method. [d] Determined by ICP analysis on the properly digested samples. [e] Determined by XPS analysis. [f] Determined by high resolution XPS N 1s core region and its relative peak deconvolution.

To get additional details on the effective nature of the iron species in **1**$^{\mathbf{N}}$, to address properly the nature of their coordination sphere and fix the nature of the metal-active sites engaged in ORR (*vide infra*), **1**$^{\mathbf{N}}$ was investigated by XAFS spectroscopy. Figures 5A-B refer to the *ex-situ* X-ray absorption near edge structure (XANES) spectra at the Fe K edge of sample **1**$^{\mathbf{N}}$ along with that of common iron oxides and metallic iron as reference samples at comparison.

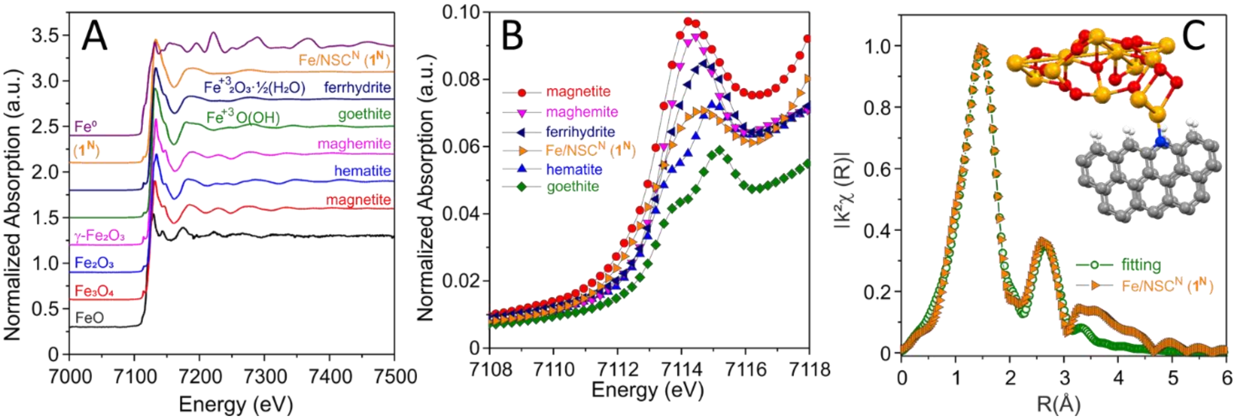

Figure 5. (A) Normalized XANES spectra for 1N and more common iron oxide samples or metallic iron. (B) Magnification section of Figure 5A dealing with the absorption pre-edge (1s → 3d) resonances. (C) k^2 weighted Fourier transform of EXAFS data of **1**$^{\mathbf{N}}$ and related fit. Color codes for the inset: C = gray, H= white, N= blue, Fe = orange, O = red

A careful analysis of Figure 5A reveals a striking match between ferrihydrite (*Fh*)[50] and our sample **1**$^{\mathbf{N}}$. Even if the former may be present in several forms and crystallinity, all of them share similar structural features such as the prevalence of six coordinated Fe^{III} centers and distinct Fe-Fe second and third shells distributed around 3.0 and 3.4Å. A closer look to the pre-edge peak (1s → 3d transition) in Figure 5B confirms that **1**$^{\mathbf{N}}$ contains prevalently Fe^{III}. While the positions of the absorption pre-edge (1s → 3d) as well as that of the edge peak (1s → 4p transition) resonances are sensitive to the iron oxidation state, the intensity of the 1s → 3d transition depends on the site symmetry: in particular, the lower the transition intensity the higher the centrosymmetric character of the iron site. Therefore, intense pre-edge peaks will account for tetrahedral or distorted octahedral geometries while octahedral coordination environments give rise to less intense signals.

As Figure 5B shows, the pre-edge resonance in **1^N** well align with maghemite (γ-Fe_2O_3) and ferrihydrite ($Fe_2O_3{\cdot}½H_2O$, *Fh*) with a peak intensity[51] evidently lower than that of other partially four coordinated compounds. This feature clearly suggests a prevalent six coordination sphere around the metal center. Finally, a quantitative evaluation of the local structure has been performed by fitting the Fe K edge EXAFS signal (see Figure 5C and Figure S5) and structural data are reported in Table 2.

Table 2. Structural data from the fitting of **1^N** Fe K-edge EXAFS signal.

Path	Coord. Numb.	R(Å)^a	σ^2 (10^{-2} Å^2)^b	ΔE_0 ^{c}	R-factor ^{d}
Fe-O(N)	6.2 (6)	1.957 (7)	1.2 (1)	-5 (1)	0.007
Fe-Fe (1)	1.3 (3)	3.00 (1)	-	-	-
Fe-Fe (2)	1.6 (4)	3.45 (2)	-	-	-

^{a} Interatomic distance. ^{b} Debye-Waller factor. ^{c} Difference in the threshold Fermi level between data and fit. ^{d} Goodness of fit parameters.

If the signal fitting establishes a coordination very close to that expected for ferrihydrite (*Fh*),[50] with a *hcp* form of Fe oxyhydroxide, where Fe^{III} cations are coordinated with O atoms and terminal OH species, Fe-Fe(1,2) coordination numbers are appreciably lower (1.3 and 1.6, respectively) than those expected for bulk ferrihydrite[50] or crystallized goethite[52] whose Fe-Fe(1) and Fe-Fe(2) values are roughly estimated in 4 and 6, respectively. This structural features found a pretty good match between data recorded for **1^N** and previously reported data on N-coordinated iron sites (Fe-N-C) as single atoms or polyatomic species at the interface between iron oxyhydroxide and a nitrogen-doped carbon network.[17] In their seminal contribution, Arrigo, R. *et al*. concluded on the structural nature of their N-coordinated iron sites and their catalytic performance in the CO_2 electrochemical reduction (CO_2RR) by the combination of operando XAFS analysis and *in-silico* studies. These authors demonstrated that their iron active-sites were not directly embedded in a nitrogen doped C-network but they were present as small *Fh*-FeOOH clusters or Fe single atoms at the edge of N-doped graphitic frameworks (*inset* Figure 5C). It should be stressed that EXAFS cannot establish if N or O are mixed in the first shell, since scattering amplitudes and phases are very similar. Anyhow, a fit with only N-coordinative sites would result into a too large coordination number. According to XPS evidences for the presence of a Fe-N component in the fitting of the N 1s high resolution peak (see Figure 3C) and the last NH_3 thermo-chemical treatment $\mathbf{1^N}$ underwent, it can be inferred that active iron sites of the latter possess a mixed N, O coordination environment. The Debye Waller factor reported in Table 2 is enough large as to confirm a distribution of distances in the octahedron (0.01Å^2). However, the introduction of two distinct Fe-O, N sub shells does not improve the fit at all: the octahedron is deformed, but the contributions cannot be resolved.

All these data taken together confirm the role of KSCN in the starting mixture to get highly dispersed Fe-N-C nuclei at the interface between an iron oxyhydroxide nanostructure and a nitrogen-doped carbon network almost exclusively in the final composite. The addition of $^-$SCN ions was found to prevent the generation of iron carbides to a larger extent,[24] while favoring the conversion of the excess of iron (not present as dispersed Fe-N-C nuclei of the type described above) into iron sulfides[24] that were leached and easily removed upon the acid washing step.

These results agree with the XRD pattern recorded for $\mathbf{2^w}$ and $\mathbf{1^w}$ (Figure 2B). Indeed, diffraction peaks ascribed to residual Fe_3C and metallic Fe species still survive on the leached $\mathbf{2^w}$ sample while their intensity is no longer appreciable on $\mathbf{1^w}$ counterpart. Finally, the presence of residual and acid-resistant iron clusters can be ascribed - in part at least - to the adopted synthetic methodology and hence to the tendency of the iron aggregates to be formed in the material bulk and thus to be protected/encapsulated within carbon shells which may prevent their effective acid etching and removal during the washing phase. This also explains the persistence of iron oxyhydroxide sub-nanometric structures of the type detected in $\mathbf{1^N}$ whose exposure to the catalyst surface is a direct consequence of the N-doped carbon shells etching and removal, promoted by the final NH_3 thermochemical treatment.

As far as the iron loading in $\mathbf{1^N}$ and $\mathbf{2^N}$ is concerned, a semi-quantitative estimation based on XPS analyses has predicted a higher metal content in $\mathbf{1^N}$ (1.7 at. %) than that measured in $\mathbf{2^N}$ (0.92 at.%). A quantitative metal content for the two samples was finally determined by inductively coupled plasma atomic emission spectroscopy (ICP-AES) and it was fixed to 2.54 and 1.67 wt.% in $\mathbf{1^N}$ and $\mathbf{2^N}$, respectively. This result additionally strengthens the role of ^-SCN ion in the preparation of iron-containing samples with a relatively high metal loading available in the form (almost exclusively) of dispersed Fe-N-C nuclei between an iron oxyhydroxide nanostructure and a N-doped carbon network.

The nature, composition and morphological properties of $\mathbf{1^N}$ and $\mathbf{2^N}$ have prompted us to evaluate and compare the performance of these two samples as catalysts in a highly challenging and kinetically sluggish process at the heart of fuel cells technology like the electrocatalytic oxygen reduction reaction (ORR). As far as the ORR electrocatalytic activity of Fe_3C nanostructures similar to those present in $\mathbf{2^N}$ is concerned, their performance in the process is documented since a relatively long time. Several experimental and *in-silico* studies have demonstrated that N-doped carbon shells protecting Fe_3C clusters do not simply prevent the metal etching/leaching during the acid treatment step but interact electronically with underneath Fe_3C NPs. As a result, the outer N-doped C-layers deeply improved their O_2 adsorption capacity acting from good to excellent electrocatalysts for ORR.[53-68] On the other hand, bare Fe_3C phases directly exposed to the electrolyte showed poor ORR performance only.[55, 69]

In addition, the well-known role of N-doped C-structures to act as metal-free catalysts for the process[4-5, 19, 70-71] led us to tackle an additional comparative test between the Fe-containing samples $\mathbf{1^N}$-$\mathbf{2^N}$ and an iron-free NSC^N ($\mathbf{3^N}$) phase prepared by the same multi-step synthetic procedure used for $\mathbf{1^N}$ except for the addition of $FeCl_3 \cdot 6H_2O$ (see experimental section for details).

Similarly to other iron-based samples from this series, a chemico-morphological characterization of the metal-free $\mathbf{3^N}$ has been accomplished and outlined in Table 1 and Figure S6A-C. A direct comparison of $\mathbf{1^N}$, $\mathbf{2^N}$ and $\mathbf{3^N}$ with the benchmark Pt/C (20 wt.%, **4**) was finally carried out for the sake of completeness under comparable (alkaline environment) experimental conditions, using the same electrochemical set-up.

A comparative screening with most relevant outcomes selected from the recent literature on related systems has also been accomplished to better highlight the excellent performance of our Fe-N-C catalyst ($\mathbf{1^N}$) in the process.

Electrochemical tests on Fe/NSC^N ($\mathbf{1^N}$)*, Fe/NC^N* ($\mathbf{2^N}$)*, NSC^N* ($\mathbf{3^N}$) *and Pt/C* (**4**) *as ORR electrocatalysts under alkaline environment.*

All catalytic materials were prepared as Nafion-containing inks to be casted on the glassy carbon (GC) of a rotating ring disk electrode (RRDE) to give - after evaporation at room temperature - a thin and homogeneous catalytic film for electrochemical tests (see Experimental Section). For $\mathbf{1^N}$-$\mathbf{2^N}$ and $\mathbf{3^N}$, the amount of the deposited catalyst was conventionally fixed to 750 $\mu g\ cm^{-2}$ irrespective to the Fe loading measured on each sample (2.54 wt.% for $\mathbf{1^N}$; 1.67 wt.% for $\mathbf{2^N}$ and 0.0 wt.% for $\mathbf{3^N}$; see also Table 1). The as-prepared electrocatalysts were conventionally investigated at various rotating speed of the working electrode in a O_2-saturated, 0.1 M KOH solution, using a typical three-electrode cell. Potential (E) values were finally reversed against the reversible hydrogen electrode (RHE) considering the pH of the solution after O_2 saturation (pH ~

13).

Figure 6A illustrates the ORR polarization curves of electrocatalysts $\mathbf{1^N}$-$\mathbf{3^N}$ and **4** at comparison. For all ORR profiles, background currents measured under N_2-saturated conditions were subtracted from the respective curves to eliminate all capacitive contributions. Worthy of note, the onset potential value (E_{on}) measured for $\mathbf{1^N}$ was shifted of roughly 100 mV to lower overpotentials respect to Pt/C (**4**) with E_{on} values for $\mathbf{2^N}$ and the metal-free ($\mathbf{3^N}$) electrocatalysts being shifted instead to more reducing potentials (≈ - 80 and ≈ - 60 mV, respectively) respect to the Pt-benchmark system (see also Table 3). Accordingly, ORR started on $\mathbf{1^N}$ at + 1.14 V *vs*. RHE with a positive overpotential of ≈100 mV compared to Pt/C (**4**) and up to ≈ 200 mV respect to the less performing iron-based system $\mathbf{2^N}$ from this series. $\mathbf{1^N}$ largely outperformed $\mathbf{2^N}$ as well as its metal-free counterpart $\mathbf{3^N}$ showing the closest current density values to those measured on **4** at the higher overpotentials (Figure 6A). The important activity gap measured between the two iron-based electrocatalysts $\mathbf{1^N}$ and $\mathbf{2^N}$ (Figure 6A) was not simply ascribed to the lower Fe-loading in $\mathbf{2^N}$ (Table 1) but rather to the different nature of the metal active sites in the samples. At odds with literature reports where iron carbide particles encapsulated in N-doped C-networks are invoked as the active sites for ORR, composition and morphology of the iron species in $\mathbf{1^N}$ and $\mathbf{2^N}$ suggest a different story.

The exclusive presence of Fe-N-C moieties between an iron oxyhydroxide nanostructure and a N-doped carbon network in $\mathbf{1^N}$ is certainly at the origin of its superior ORR performance. Moreover, the high-temperature ammonia treatment on $\mathbf{1^w}$ and $\mathbf{2^w}$ deeply etches and remove the N-doped carbon shells protecting the Fe_3C nanoclusters (particularly in $\mathbf{2^N}$ where they are present to a larger extent), exposing them to the electrolyte solution and hence reducing the electrocatalyst performance in the process.

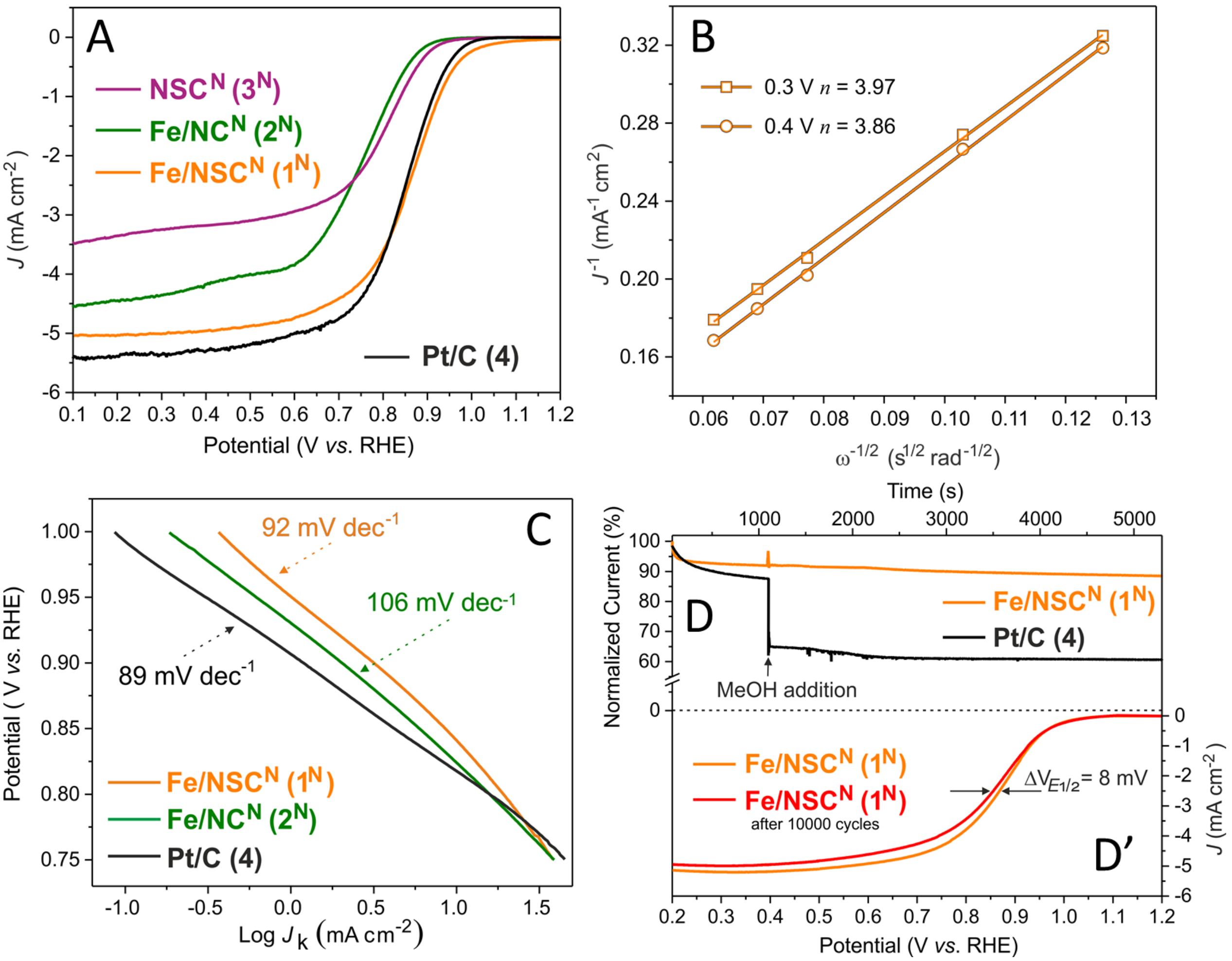

Figure 6. (A) Steady-state polarization curves of **1^N-3^N** and **4** recorded in an O_2-saturated 0.1 M KOH electrolyte solution at a scan rate of 5 mV s^{-1} at a rotating speed of the working electrode of 1600 rpm; (B) K-L plots for **1^N** as obtained from the respective LSVs at 0.3-0.4 V. Parameters used: O_2 concentration (C_0), 1.15×10^{-3} mol L^{-1}; O_2 diffusion coefficient (D_0), 1.95×10^{-5} cm^2 s^{-1}; kinematic viscosity (v) of the electrolyte solution, 0.008977 cm^2 s^{-1}; (C) Tafel plots for **1^N**, **2^N** and **4**; (D) catalysts poisoning and (D') durability tests.

Finally, the superior performance of **1^N** respect to its metal-free counterpart **3^N** (Figure 6A, Table 3 entry 1 *vs*. 3) additionally emphasizes the existence of a synergistic and positive action between the atomically dispersed metal ions and the N-sites in the hosting C-network.

The average number of electrons ($n_{E\ (V)}$) transferred for O_2 molecule in the process has been finally determined for the most performing catalyst (**1^N**) according to the Koutecky-Levich (K-L) equation.[72] Values calculated at variable potentials (E = 0.3-0.7 V) are outlined in Figure 6B,

Figure S7B and summarized on Table 3. K−L plots (J^{-1} *vs.* $\omega^{-1/2}$) of **1^{N}**, obtained from Linear-Swept-Voltammograms (LSVs, Figure S7A) according to *J* values measured in the 0.3-0.7 V range, show good linearity at various rotation speeds (Figure 6B and Figure S7B), hence implying a first order reaction toward dissolved O_2. As Figure 6B and Table 3 show, n_E values suggest a largely prevailing four-electron process with **1^{N}** whatever the potential value (in the 0.3-0.7 V range) at which *J* was measured (Figure S7A). This result was additionally corroborated by the moderate ring current value measured for **1^{N}** at the Pt ring of the rotating ring-disk electrode (RRDE). Such a moderate value accounts for an equally moderate H_2O_2 production with **1^{N}** respect to **2^{N}** and **3^{N}** under identical experimental conditions (Figure S7C).[73]

Additional kinetic data (Figure 6C and Table 3) have been used to remark the excellent ORR performance of **1^{N}** compared to the other catalytic system from the same series (**2^{N}**). They have been finally used to unveil the close behavior of **1^{N}** with the benchmark Pt-based catalyst of the *state-of-the-art* (**4**). Indeed, by fitting the linear portion of Tafel plots (Figure 6C) recorded for **1^{N}**, **2^{N}** and **4**, we have extrapolated important electrochemical parameters such as the Tafel slope (mV dec^{-1}).[74-75] Tafel slopes values are listed in the Table 3. A Tafel slope of 92 mV dec^{-1} has been measured for **1^{N}**, a value appreciably lower than that obtained with **2^{N}** (106 mV dec^{-1}) and quite close to that of the Pt benchmark system (89 mV dec^{-1}). Finally, the kinetic current density (J_k) measured on **1^{N}** (8.43 mA cm^{-2} @0.85 V) was twice higher than that measured on Pt/C (4.19 mA cm^{-2} @0.85 V) and ranked appreciably higher than that measured on **2^{N}** (5.86 mA cm^{-2} @0.85 V).

Table 3. Electrochemical performance of catalysts **1^{N}-3^{N}** and **4** in ORR

Entry	Catalyst	E_{on} [a] (V)	$E_{1/2}$ [a] (V)	n_E [b]	Tafel slope (mV dec^{-1})	J_k [c] (mA cm^{-2})
1	Fe/NSC^{N} (**1^{N}**)	1.14	0.87	3.97	92	8.43

2	Fe/NC$^{\mathrm{N}}$ (**2**$^{\mathrm{N}}$)	0.94	0.75	-	106	5.86
3	NSC$^{\mathrm{N}}$ (**3**$^{\mathrm{N}}$)	0.96	0.82	-	n.d.	n.d.
4	Pt/C (**4**)	1.02	0.85	-	89	4.19

[a] Potential values reported *vs*. RHE [b] calculated from K-L equation at 0.3 V *vs*. RHE [c] calculated at 0.85 V *vs*. RHE.

As an additional trial, the tolerance of the best performing iron-based electrocatalyst from this series towards alcohol poisoning has been investigated. Methanol tolerance is a fundamental prerequisite for the successful exploitation of these electrocatalysts at the cathode of direct methanol fuel cells (DMFC).[76] However, fuel crossover through the polymeric electrolyte membrane (from the anode to the cathode side) is known to compromise the overall fuel cell performance by deeply affecting performance of Pt-based electrocatalysts.[77] Accordingly, ORR was operated with Fe/NSC$^{\mathrm{N}}$ (**1**$^{\mathrm{N}}$) and the benchmark Pt/C (**4**) and their electrochemical solutions were treated in one portion with methanol (1 % v/v; Figure 6D). Upon the alcohol addition, **1**$^{\mathrm{N}}$ maintains its performance almost unchanged while J on Pt/C (**4**) dropped down rapidly as a consequence of the undesired methanol oxidation and irreversible catalyst poisoning.[78-79] Finally, long-term cycling RRDE measurements in the 0.2 ÷ 1.2 V range at the rate of 50 mV s^{-1}, 1600 rpm in a 0.1 M KOH solution at room temperature, have been carried out in order to investigate the stability of **1**$^{\mathrm{N}}$ under the electrochemical conditions. As Figure 6D' shows, only a moderate decrease of J (< 4% measured at 0.2 V) takes place after 10000 electrochemical cycles together with an equally moderate decrease of the $E_{1/2}$ (estimated in about 8 mV), whereas E_{on} remains unchanged thus confirming the excellent stability of the electrocatalyst for the process under the adopted experimental conditions.

In spite of the plethora of related synthetic protocols discussed in the literature so far and focused on the development of SACs for electrocatalysis, the effective, straightforward and sustainable character of our synthetic scheme towards the preparation of highly dispersed Fe-N-C based catalysts, lays the groundworks for its further exploitation in combination with different non-noble metal precursors. Moreover, the performance of the as-prepared catalysts in a challenging electrochemical process (*i.e.* ORR), highlights the unique potentialities of an effective protocol for the homogeneous dispersion of Fe-N-C active sites. Although we are aware about the difficult task of comparing the electrocatalytic features of our best performing system $\mathbf{1}^{\mathbf{N}}$ with other related SACs in the process, we feel that a concise comparison with the most representative Fe/SACs reported in the literature so far will be the most useful tool in hands of our readerships to better appreciate the performance of our synthetic protocol and compare the as-prepared SACs with related systems operated under similar electrochemical conditions. With this aim, Table S1 lists more than 100 examples of variably prepared Fe-SACs appeared in the recent years and selected among the most performing electrocatalysts for the ORR under alkaline environment. A careful analysis of the main electrochemical features of these Fe-based SACs, unveils that $\mathbf{1}^{\mathbf{N}}$ certainly ranks among the most performing ORR systems reported in the literature up to date. With E_{on} and $E_{1/2}$ values among the highest reported to date, the prevalent $4e^-$ reduction nature of the process at work with this SAC and the extremely clean and effective control towards the generation of highly-loaded and atomically dispersed catalysts, the proposed methodology sounds a promising tool for the benchmarking of various non-noble metal-based SACs.

Conclusions

In summary, we have described an effective and general strategy to the clean production of highly metal charged Fe-based composites containing discrete Fe-N-C moieties at the interface of iron oxyhydroxide sub-nanometric structures and a N-doped carbon network through the combination of chelating citrate ions with the ancillary monodentate $^{-}$SCN ligand. The control of the metal ion donor atom set originates an ideal "open gate" for water soluble iron ions to be accommodated in the form of Fe-N-C moieties within final C-N networks. A rational exploitation of their thermo-chemical and washing sequences has finally provided an effective and durable electrocatalyst for promoting the kinetically sluggish oxygen reduction reaction. Besides the general synthetic scheme that may apply to a variety of water-soluble transition-metal based salts, the protocol is a cost-effective path to the clean production of iron-composites containing catalytically active Fe-N-C moieties for the electrochemical process. The as-prepared highly metal-loaded catalyst has shown electrocatalytic performance under alkaline environment that ranks among the highest reported so far for related Fe-SACs of the state-of-the-art. Studies devoted to the preparation and characterization of different transition metal SACs based on the functional protocol described in the paper are currently on-going in the lab and will be reported elsewhere in combination with different catalytic applications.

Experimental Section

Materials and Methods

D-glucose [$C_6H_{12}O_6$, 100 %, MW: 180.16 g mol^{-1}], citric acid [$C_6H_8O_7$ anhydrous, > 99.5 %, MW: 192.12 g mol^{-1}] and ammonium carbonate [$(NH_4)_2CO_3$, MW: 96.09 g mol^{-1}], were provided by ACROS Organic^{TM}, MYPROTEIN^{TM} and VWR Chemicals, respectively. Potassium thiocyanate (KSCN > 97 %; MW: 97.18 g mol^{-1}), Iron (III) chloride hexahydrate ($FeCl_3 \cdot 6H_2O$ > 98%, MW: 270.30 g mol^{-1}) and Nafion® (5 wt. % in isopropanol and water) were obtained from Merck and Fluka. Unless otherwise stated, all reagents and solvents were used as provided by commercial suppliers without any further purification/treatment.

Scanning Electron Microscopy (SEM) analyses were carried out on a Zeiss 2600F with a resolution of 5 nm. Samples were deposited onto a double face graphite tape in order to avoid charging effects during the measurements. *Transmission Electron Microscopy* (TEM) was carried out on a JEOL 2100F working at 200 kV accelerated voltage, equipped with a probe corrector for spherical aberrations and a point-to-point resolution of 0.2 nm. *X-ray Photoelectron Spectroscopy* (XPS) was conducted either in an ultrahigh vacuum (UHV) spectrometer equipped with a VSW Class WA hemispherical electron analyzer or in an ultrahigh vacuum (UHV) Thermo-VG Scientific spectrometer equipped with a CLAM4 (MCD) hemispherical electron analyzer. A monochromatic Al Kα X-ray source (1486.6 eV) or a non-monochromated Mg Kα X-ray source (1253.6 eV) was used as incident radiation. Survey and high-resolution spectra were recorded in constant pass energy mode (90 and 44 eV, respectively). High resolution XPS peaks deconvolution has been accomplished with mixed Gaussian-Lorentzian curves using XPS Peak 4.1 software minimizing the mean squared error. *X-ray* diffractograms were recorded using Cu Kα radiation (40 mA, 45 kV) in the 10-80º 2θ range, using step size and step time of 0.05° and 80 s, respectively. The pore structural property of the different samples determined by N_2-physisorption at 77 K with a Micromeritics Tristar II instrument (Micromeritics GmbH, Munich, Germany). Before measurement, the sample was outgassed at 200 ºC under vacuum overnight. Specific Surface Area (SSA) values were assessed with Brunauer-Emmett-Teller (BET) model while pore size distribution was evaluated from the adsorption branch of N_2 isotherms following the (Barrett-Joyner-Halenda) BJH method. *Elemental analyses* were carried out on a Thermo FlashEA 1112 Series CHNS-O elemental analyzer and elemental average values were calculated over three independent runs. *XAFS measurements and analysis*. XAFS data were collected in transmission on beamline SAMBA (Synchrotron SOLEIL, France)[80] using a sagittally bending Si 220 monochromator, a pair of Pd mirrors at 4.5 mrad for harmonic rejection and ionization chambers as intensity monitors placed before and after the sample and a reference metallic iron foil. The sample was prepared as a pellet using cellulose as a binder. Data analysis was performed using the package Horae.[81] Theoretical standards were computed over a maghemite model. Only one Debye Waller factor for all paths was found to be necessary and only one common energy shift was allowed to float. Data were simulated from 3 to 12 Å^{-1} in k space and from 1 to 3.5 Å in r-space, data were k^3-weighted.

*Preparation of Fe/NSC^N (**1^N**), Fe/NC^N (**2^N**) and the metal-free NSC^N (**3^N**) catalysts*. In a typical procedure to Fe/NSC^N (**1^N**) a solid mixture made of 1 g of D-glucose (5.55 mmol), 1.5 g of citric acid (7.81 mmol), 1.5 g of $(NH_4)_2CO_3$ (15.61 mmol) and 0.1566 g of KSCN (1.61 mmol) was dissolved at room temperature in 25 mL of ultrapure water (Veolia Ultra Analytique, 18.2 MΩxcm, TOC < 2 ppb). Afterwards, 0.1452 g of $FeCl_3 \cdot 6H_2O$ (0.537 mmol) in 3 mL of water were added dropwise to the aforementioned solution and the resulting mixture was stirred at r.t. for further 30 min. A hygroscopic brownish gel (Fe/NSC^g, **1^g**) was isolated after water evaporation in an oven at 110 °C overnight. The latter was then pyrolyzed at 900 °C under Ar atmosphere for 1 h (program temperature ramp: 5 °C min^{-1}) to give a dark-brown powder (Fe/NSC^p, **1^p**) that was treated with a 0.5 M H_2SO_4 solution at 80 °C for 8 h during which unreactive iron species were leached, leaving behind a reddish material that was thoroughly washed with deionized water till neutrality (pH = 7) of the washing phases. The as-obtained sample (Fe/NSC^w, **1^w**) was then rinsed with ethanol and evaporated to dryness overnight at 75 °C before being reacted with NH_3 at 900 °C for 10 min. The resulting dark-black material (Fe/NSC^N, **1^N**) was then employed as such for the preparation of the ink to be used in the electrochemical catalytic tests (*vide infra*). The loading amount of Fe in Fe/NSC^N was determined by inductively coupled plasma-atomic emission spectroscopy (ICP-

AES, Plasma-Spec-2 * ROMAN spectrometer) and it was fixed in 25.44 g kg^{-1}_{cat}, *i.e.* of 2.54 wt %.

As far as the preparation of Fe/NC^N and the metal-free NSC^N samples is concerned, multi-steps procedures identical to that described above were employed except for the use of KSCN (for Fe/NC^N, $\mathbf{2^N}$) and the addition of $FeCl_3{\cdot}6H_2O$ (for NSC^N, $\mathbf{3^N}$). Most relevant characterization features for the last two samples are discussed and reported throughout the Results and Discussion session.

Electrochemical measurements. 6 mg of Fe/NSC^N ($\mathbf{1^N}$), Fe/NC^N ($\mathbf{2^N}$) or NSC^N ($\mathbf{3^N}$) were dispersed in a 0.4 mL solution of ethanol (0.1 mL) in ultrapure water (0.3 mL - Veolia, Ultra Analitique, 18.2 MOhm.cm, TOC<1 ppb). 15 μL of a Nafion® solution (5 wt. % isopropanol and water) were then used as binder and were added to the above prepared suspension. The latter was treated in an ultrasonic bath till a homogeneous dark-black ink was formed. Afterwards, 10 μL of the ink were drop-casted on the glassy carbon surface of a rotating-ring disk electrode (RRDE, PINE AFE6R2GCPT, glassy carbon disk with a diameter of 5 mm, Pt ring with inner diameter of 6 mm and outer diameter of 8 mm), and dried at room temperature. The casting/drying procedure was repeated till the GC surface was charged with 750 μg cm^{-2} of the catalyst. Such a catalyst loading was assumed in accord with the highest number of exchanged electrons measured on the most performing system from this series ($\mathbf{1^N}$) at variable catalyst ink loadings. The as prepared electrocatalyst was employed as working electrode in a three-electrode cell equipped with Hg/HgO and Pt foil as reference and counter electrode, respectively. Any potential Pt leaching from counter electrode (even if not much favored in alkaline media)[82] has been excluded by XPS analysis conducted on sample $\mathbf{1^N}$ recovered after electrocatalysis (Figure S8). All potentials were calibrated to reversible hydrogen electrode (RHE). Linear sweep voltammetry (LSV) was conducted in O_2-

saturated 0.1 M KOH electrolyte solution in the 0.2 - 1.2 V range at a scan rate of 10 mV s^{-1} with a rotating electrode rate of 1600 rpm and the ring potential was kept at 1.2 V *vs*. RHE.

For a comparative analysis, Pt/C (**4**) (Johnson-Matthey, 20 wt.%) was employed as benchmark system with a Pt loading of 20 µg cm^{-2}. Finally, methanol poisoning experiments were conducted under an O_2-saturated 0.1 M KOH solution upon addition of 1 % (v:v) of MeOH. The number of electrons involved in the oxygen reduction process (ORR) were calculated from the Koutecky-Levich equation as follows:

$$\frac{1}{J} = \frac{1}{J_L} + \frac{1}{J_K} = \frac{1}{B\omega^{1/2}} + \frac{1}{J_K}$$

$$B = 0.62nFC_O {D_O}^{2/3} \upsilon^{-1/6}$$

where J is the measured current density, J_K and J_L are the kinetic and diffusion-limiting current densities respectively, ω is the angular velocity (rad/s), n is a number of electrons in ORR reaction, F is the Faraday constant (96485 C · mol^{-1}), C_o is the bulk concentration of O_2 (1.2×10^{-6} mol·cm^{-3}), D_o is the diffusion coefficient of O_2 in 0.1 M KOH (1.9×10^{-5} $cm^2 \cdot s^{-1}$), and υ is the kinetic viscosity of the electrolyte (0.01 $cm^2 \cdot s^{-1}$).

Kinetic current density was also calculated at 0.85 V from the following equation:

$$J_k = \frac{J_L \times J}{J_L - \mathrm{J}}$$

Author Information

Corresponding Authors

* E-mail: giambastiani@unistra.fr

* E-mail: sergey.pronkin@unistra.fr

* E-mail: cuong.pham-huu@unistra.fr

Notes

The authors declare no competing financial interest.

Associated Content

Supporting Information: Additional Figures; XPS, TEM and elemental mapping for **1**$^{\mathbf{N}}$, **2**$^{\mathbf{N}}$ and **3**$^{\mathbf{N}}$; k^2 weighted Fe K edge EXAFS signal of **1**$^{\mathbf{N}}$ and its fitting; Fourier transform **1**$^{\mathbf{N}}$ EXAFS; Nitrogen adsorption-desorption isotherm linear plots (BET) of **3**$^{\mathbf{N}}$. Linear sweep voltammograms (LSVs) of **1**$^{\mathbf{N}}$ and the relative K-L plots. RRDE current-potential curves measured for all electrocatalysts from this series. This material is available free of charge via the Internet at http://pubs.acs.org.

Acknowledgements

G. G. and C. P.-H. thank the TRAINER project (Catalysts for Transition to Renewable Energy Future) of the “Make our Planet Great Again” program (Ref. ANR-17-MPGA-0017) for support. The Italian teams would also like to thank the Italian MIUR through the PRIN 2017 Project Multi-e (20179337R7) “Multielectron transfer for the conversion of small molecules: an enabling technology for the chemical use of renewable energy” for financial support to this work. S. P. is grateful for financial support from Institut Carno MICA (exploratory research project COM-Gra 2020). X. Z. also thanks the China Scholarship Council (CSC) for financial support to his PhD at the ICPEES-CNRS.

References and Notes

1. Huang, Z.-F.; Wang, J.; Peng, Y.; Jung, C.-Y.; Fisher, A.; Wang, X., Design of Efficient Bifunctional Oxygen Reduction/Evolution Electrocatalyst: Recent Advances and

Perspectives. *Adv. Energy Mater.* **2017**, *7*, 1700544 (21).

2. Wagner, F. T.; Lakshmanan, B.; Mathias, M. F., Electrochemistry and the future of the automobile. *J. Phys. Chem. Lett.* **2010**, *1*, 2204-2219.
3. Wang, X.; Li, Z.; Qu, Y.; Yuan, T.; Wang, W.; Wu, Y.; Li, Y., Review of Metal Catalysts for Oxygen Reduction Reaction: From Nanoscale Engineering to Atomic Design. *Chem* **2019**, *5*, 1486-1511.
4. Ma, R.; Lin, G.; Zhou, Y.; Liu, Q.; Zhang, T.; Shan, G.; Yang, M.; Wang, J., A review of oxygen reduction mechanisms for metal-free carbon-based electrocatalysts. *Npj Comput. Mater.* **2019**, *5*, 78 (15).
5. Dai, L.; Xue, Y.; Qu, L.; Choi, H.-J.; Baek, J.-B., Metal-Free Catalysts for Oxygen Reduction Reaction. *Chem. Rev.* **2015**, *115*, 4823-4892.
6. Shao, M.; Chang, Q.; Dodelet, J.-P.; Chenitz, R., Recent Advances in Electrocatalysts for Oxygen Reduction Reaction. *Chem. Rev.* **2016**, *116*, 3594-3657.
7. Berger, D. J., Fuel Cells and Precious-Metal Catalysts. *Science* **1999**, *286*, 49.
8. Hayes, S. M.; McCullough, E. A., Critical minerals: A review of elemental trends in comprehensive criticality studies. *Resour. Policy* **2018**, *59*, 192-199.
9. Singh, B.; Sharma, V.; Gaikwad, R. P.; Fornasiero, P.; Zboril, R.; Gawande, M. B., Single-Atom Catalysts: A Sustainable Pathway for the Advanced Catalytic Applications. *Small* **2021**, *17*, 2006473 (27).
10. Gawande, M. B.; Fornasiero, P.; Zbořil, R., Carbon-Based Single-Atom Catalysts for Advanced Applications. *ACS Catal.* **2020**, *10*, 2231–2259.
11. Kaiser, S. K.; Chen, Z.; Akl, D. F.; Mitchell, S.; Pérez-Ramírez, J., Single-Atom Catalysts across the Periodic Table. *Chem. Rev.* **2020**, *120*, 11703-11809.

12. Hannagan, R. T.; Giannakakis, G.; Flytzani-Stephanopoulos, M.; Sykes, E. C. H., Single-Atom Alloy Catalysis. *Chem. Rev.* **2020**, *120*, 12044-12088.

13. Su, J.; Ge, R.; Dong, Y.; Hao, F.; Chen, L., Recent progress in single-atom electrocatalysts: concept, synthesis, and applications in clean energy conversion. *J. Mater. Chem. A* **2018**, *6*, 14025-14042.

14. He, Y.; Liu, S.; Priest, C.; Shi, Q.; Wu, G., Atomically dispersed metal–nitrogen–carbon catalysts for fuel cells: advances in catalyst design, electrode performance, and durability improvement. *Chem. Soc. Rev.* **2020**, *49*, 3484-3524.

15. Kou, Z.; Zang, W.; Ma, Y.; Pan, Z.; Mu, S.; Gao, X.; Tang, B.; Xiong, M.; Zhao, X.; Cheetham, A. K.; Zheng, L.; Wang, J., Cage-confinement pyrolysis route to size-controlled molybdenum-based oxygen electrode catalysts: From isolated atoms to clusters and nanoparticles. *Nano Energy* **2020**, *67*, 104288 (9).

16. Chen, Y.; ji, S.; Chen, C.; Peng, Q.; Wang, D.; Li, Y., Single-Atom Catalysts: Synthetic Strategies and Electrochemical Applications. *Joule* **2018**, *2*, 1242-1264.

17. Genovese, C.; Schuster, M. E.; Gibson, E. K.; Gianolio, D.; Posligua, V.; Grau-Crespo, R.; Cibin, G.; Wells, P. P.; Garai, D.; Solokha, V.; Calderon, S. K.; Velasco-Velez, J. J.; Ampelli, C.; Perathoner, S.; Held, G.; Centi, G.; Arrigo, R., Operando spectroscopy study of the carbon dioxide electro-reduction by iron species on nitrogen-doped carbon. *Nat. Commun.* **2018**, *9*, 935 (12).

18. Ba, H.; Liu, Y.; Truong-Phuoc, L.; Duong-Viet, C.; Mu, X.; Doh, W. H.; Tran-Thanh, T.; Baaziz, W.; Nguyen-Dinh, L.; Nhut, J.-M.; Janowska, I.; Begin, D.; Zafeiratos, S.; Granger, P.; Tuci, G.; Giambastiani, G.; Banhart, F.; Ledoux, M. J.; Pham-Huu, C., A highly N-doped carbon phase ‘‘dressing’’ of macroscopic supports for catalytic applications. *Chem. Commun.*

2015, *51*, 14393-14396.

19. Ba, H.; Liu, Y.; Truong-Phuoc, L.; Duong-Viet, C.; Nhut, J.-M.; Nguyen-Dinh, L.; Ersen, O.; Tuci, G.; Giambastiani, G.; Pham-Huu, C., N-Doped Food-Grade-Derived 3D Mesoporous Foams as Metal-Free Systems for Catalysis. *ACS Catal.* **2016**, *6*, 1408-1419.
20. Pham-Huu, C.; Giambastiani, G.; Liu, Y.; Ba, H.; Nguyen-Dinh, L.; Nhut, J.-M. Method for preparing highly nitrogen-doped mesoporous carbon composites. EP 3047905 A1, **2016**.
21. Ba, H.; Luo, J.; Liu, Y.; Duong-Viet, C.; Tuci, G.; Giambastiani, G.; Nhut, J.-M.; Nguyen-Dinh, L.; Ersen, O.; Su, D. S.; Pham-Huu, C., Macroscopically Shaped Monolith of Nanodiamonds @ Nitrogen-enriched Mesoporous Carbon Decorated SiC as a Superior Metal-free Catalyst for the Styrene Production. *Appl. Catal. B: Environ.* **2017**, *200*, 343-350.
22. Duong-Viet, C.; Nhut, J.-M.; Truong-Huu, T.; Tuci, G.; Nguyen-Dinh, L.; Liu, Y.; Pham, C.; Giambastiani, G.; Pham-Huu, C., A Nitrogen-Doped Carbon Coated Silicon Carbide as a Robust and Highly Efficient Metal-Free Catalyst for Sour Gases Desulfurization in the Presence of Aromatics as Contaminants. *Catal. Sci. Technol.* **2020**, *10*, 5487-5500.
23. Duong-Viet, C.; Nhut, J.-M.; Truong-Huu, T.; Tuci, G.; Nguyen-Dinh, L.; Pham, C.; Giambastiani, G.; Pham-Huu, C., Tailoring Properties of Metal-Free Catalysts for the Highly Efficient Desulfurization of Sour Gases under Harsh Conditions. *Catalysts* **2021**, *11*, 226 (15).
24. Chen, P.; Zhou, T.; Xing, L.; Xu, K.; Tong, Y.; Xie, H.; Zhang, L.; Yan, W.; Chu, W.; Wu, C.; Xie, Y., Atomically Dispersed Iron–Nitrogen Species as Electrocatalysts for Bifunctional Oxygen Evolution and Reduction Reactions. *Angew. Chem. Int. Ed.* **2016**, *56*, 610-614.
25. Wang, Y.-C.; Lai, Y.-J.; Song, L.; Zhou, Z.-Y.; Liu, J.-G.; Wang, Q.; Yang, X.-D.; Chen, C.; Shi, W.; Zheng, Y.-P.; Rauf, M.; Sun, S.-G., S-Doping of an Fe/N/C ORR Catalyst for Polymer Electrolyte Membrane Fuel Cells with High Power Density. *Angew. Chem. Int. Ed.* **2015**, *54*,

9907-9910.

26. Kramm, U. I.; Herrmann, I.; Fiechter, S.; Zehl, G.; Zizak, I.; Abs-Wurmbach, I.; Radnik, J.; Dorbandt, I.; Bogdanoff, P.; Trans., E.; 2009, 659 – 670., On the Influence of Sulphur on the Pyrolysis Process of FeTMPP-Cl-based Electro-Catalysts with Respect to Oxygen Reduction Reaction (ORR) in Acidic Media. *ECS Trans.* **2009**, *25*, 659-670.

27. Wang, Y.; Chen, L.; Mao, Z.; Peng, L.; Xiang, R.; Tang, X.; Deng, J.; Wei, Z.; Liao, Q., Controlled synthesis of single cobalt atom catalysts via a facile one-pot pyrolysis for efficient oxygen reduction and hydrogen evolution reactions. *Sci. Bull.* **2019**, *64*, 1095-1102.

28. Ozutsumi, K.; Kurihara, M.; Miyazawa, T.; Kawashim, T., Complexation of Iron(III) with Thiocyanate Ions in Aqueous Solution. *Anal. Sci.* **1992**, *8*, 521-526.

29. Jedrzejewska, A.; Costa, S.; Cendrowski, K.; Kalenczuk, R. J.; Mijowska, E., Synthesis and characterization of iron-filled multi-walled nanotubes. *Mater. Sci.* **2011**, *29*, 299-304.

30. Narkiewicz, U.; Guskos, N.; Arabczyk, W.; Typek, J.; Bodziony, T.; Konicki, W.; Gazsiorek, G.; Kucharewicz, I.; Anagnostakis, E. A., XRD, TEM and magnetic resonance studies of iron carbidenanoparticle agglomerates in a carbon matrix. *Carbon* **2004**, *42*, 1127-1132.

31. Tan, Y.; Zhu, K.; Li, D.; Bai, F.; Wei, Y.; Zhang, P., N-doped graphene/Fe–Fe_3C nano-composite synthesized by a Fe-basedmetal organic framework and its anode performance in lithium ionbatteries. *Chem. Eng. J.* **2014**, *258*, 93-100.

32. Huckaba, A. J.; Sanghyun, P.; Grancini, G.; Bastola, E.; Taek, C. K.; Younghui, L.; Bhandari, K. P.; Ballif, C.; Ellingson, R. J.; Nazeeruddin, M. K., Exceedingly Cheap Perovskite Solar Cells Using Iron Pyrite Hole Transport Materials. *ChemistrySelect* **2016**, *1*, 5316-5319.

33. Di Giovanni, C.; Wang, W.-A.; Nowak, S.; Grenèche, J.-M.; Lecoq, H.; Mouton, L.; Giraud, M.; Tard, C., Bioinspired Iron Sulfide Nanoparticles for Cheap and Long-Lived

Electrocatalytic Molecular Hydrogen Evolution in Neutral Water. *ACS Catal.* **2014**, *4*, 681-687.

34. Values estimated from the full width at half maximum (FWHM) of (002) carbon diffraction peaks at 2θ values of 25.9 for Fe/NSMC^W and Fe/NMC^W applied to the Scherrer Equation.
35. Sing, K. S. W.; Everett, D. H.; Haul, R. A. W.; Moscou, L.; Pierotti, R. A.; Rouquérol, J., Reporting Physisorption Data For Gas/Solid Systems with Special Reference to the Determination of Surface Area and Porosity. *Pure Appl. Chem.* **1985**, *57*, 603-619.
36. Kramm, U. I.; Herrmann-Geppert, I.; Bogdanoff, P.; Fiechter, S., Effect of an ammonia treatment on structure, composition, and oxygen reduction reaction activity of Fe-N-C catalysts. *J. Phys. Chem. C* **2011**, *115*, 23417-23427.
37. Boehm, H. P., Some aspects of the surface chemistry of carbon blacks and other carbons. *Carbon* **1994**, *32*, 759-769.
38. Perez, H.; Jorda, V.; Vigneron, J.; Frégnaux, M.; Etcheberry, A.; Quinsac, A.; Leconte, Y.; Sublemontier, O., Highly Active, High Specific Surface Area Fe/C/N ORR Electrocatalyst from Liquid Precursors by Combination of CO_2 Laser Pyrolysis and Single NH_3 Thermal Post-Treatment. *C* **2019**, *5*, 26 (15).
39. Abotsi, G. M. K.; Scaroni, A. W., Reaction of carbons with ammonia: Effects on the surface charge and molybdenum adsorption. *Carbon* **1990**, *28*, 79-84.
40. Stöhr, B.; Boehm, H. P.; Schlögl, R., Enhancement of the catalytic activity of activated carbons in oxydation reactions by thermal treatment with ammonia or hydrogen cyanide and observation of a superoxide species as a possible intermediate. *Carbon* **1991**, *29*, 707-720.
41. Artyushkova, K.; Serov, A.; Rojas-Carbonell, S.; Atanassov, P., Chemistry of Multitudinous Active Sites for Oxygen Reduction Reaction in Transition Metal−Nitrogen−Carbon

Electrocatalysts. *J. Phys. Chem. C* **2015**, *119*, 25917-25928.

42. Zhang, N.; Zhou, T.; Chen, M.; Feng, H.; Yuan, R.; Zhong, C.; Yan, W.; Tian, Y.; Wu, X.; Chu, W.; Wu, C.; Xie, Y., High-purity pyrrole-type FeN_4 sites as a superior oxygen reduction electrocatalyst. *Energy Environ. Sci.* **2020**, *13*, 111-118.
43. Sherwood, T. K.; Maak, R. O., The Reaction of Ammonia with Carbon at Elevated Temperatures. *Ind. Eng. Chem. Fundamen.* **1962**, *1*, 111-115.
44. Zitolo, A.; Goellner, V.; Armel, V.; Sougrati, M.-T.; Mineva, T.; Stievano, L.; Fonda, E.; Jaouen, F., Identification of catalytic sites for oxygen reduction in iron- and nitrogen-doped graphene materials. *Nat. Mater.* **2015**, *14*, 937-942.
45. Kramm, U. I.; Herrmann-Geppert, I.; Behrends, J.; Lips, K.; Fiechter, S.; Bogdanoff, P., On an easy way to prepare Metal-Nitrogen doped Carbon with exclusive presence of MeN_4-type sites active for the ORR. *J. Am. Chem. Soc.* **2016**, *138*, 635-640.
46. Song, C.; Wu, S.; Shen, X.; Miao, X.; Ji, Z.; Yuan, A.; Xu, K.; Liu, M.; Xie, X.; Kong, L.; Zhu, G.; Shah, S. A., Metal-organic framework derived Fe/Fe_3C@N-doped-carbon porous hierarchical polyhedrons as bifunctional electrocatalysts for hydrogen evolution and oxygen-reduction reactions. *J. Colloid Interface Sci.* **2018**, *524*, 93-101.
47. Yan, B.; Liu, Y.; Zhang, Y.; Guo, Y.; Guo, W.; Chen, L.; Yu, F.; Wang, G., Uniformly Dispersed Fe_3C (~ 5 nm) in Fe-N-Doped Carbon Nanosheets Derived from Coal Tar Pitch as Efficient Electrocatalysts for Oxygen Reduction Reaction. *Mater. Lett.* **2020**, *273*, 127861 (5).
48. Ke, M.; Qu, Q., Thermal Decomposition of Thiocyanate Corrosion Inhibitors: A Potential Problem for Successful Well Completions. In *SPE International Symposium and Exhibition on Formation Damage Control*, Lafayette: 2006; p SPE 98302.
49. Wei, Q.; Zhang, G.; Yang, X.; Fu, Y.; Yang, G.; Chen, N.; Chen, W.; Sun, S., Litchi-like porous

Fe/N/C spheres with atomically dispersed FeN_x promoted by sulfur as highly efficient oxygen electrocatalysts for Zn–air batteries. *J. Mater. Chem. A* **2018**, *6*, 4605-4610.

50. Michel, F. M.; Ehm, L.; Antao, S. M.; Lee, P. L.; Chupas, P. J.; Liu, G.; Strongin, D. R.; Schoonen, M. A. A.; Phillips, B. L.; Parise, J. B., The Structure of Ferrihydrite, a Nanocrystalline Material. *Science* **2007**, *316*, 1726-1729.
51. Petit, P.-E.; Farges, F.; Wilke, M.; Solé, V. A., Determination of the iron oxidation state in Earth materials using XANES pre-edge information. *J. Synchrotron Radiat.* **2001**, *8*, 952-954.
52. Yang, H.; Lu, R.; Downs, R. T.; Costin, G., Goethite, α-FeO (OH), from single-crystal data. *Acta Crystallogr. E* **2006**, *62*, 250-252.
53. Yang, W.; Yue, X.; Liu, X.; Chen, L.; Jia, J.; Guo, S., Superior oxygen reduction electrocatalysis enabled by integrating hierarchical pores, Fe_3C nanoparticles and bamboo-like carbon nanotubes. *Nanoscale* **2016**, *8*, 959-964.
54. Hu, Y.; Jensen, J. O.; Zhang, W.; Cleemann, L. N.; Xing, W.; Bjerrum, N. J.; Li, Q., Hollow spheres of iron carbide nanoparticles encased in graphitic layers as oxygen reduction catalysts. *Angew. Chem. Int. Ed. 53*, 3675-3679.
55. Liu, M.; Yin, X.; Guo, X.; Hu, L.; Yuan, H.; Wang, G.; Wang, F.; Chen, L.; Zhang, L.; F., Y., High efficient oxygen reduction performance of Fe/Fe_3C nanoparticles in situ encapsulated in nitrogen-doped carbon via a novel microwave-assisted carbon bath method. *Nano Mater. Sci.* **2019**, *1*, 131-136.
56. Deng, D.; Yu, L.; Chen, X.; Wang, G.; Jin, L.; Pan, X.; Deng, J.; Sun, G.; Bao, X., Iron Encapsulated within Pod-Like Carbon Nanotubes for Oxygen Reduction Reaction. *Angew. Chem. Int. Ed.* **2013**, *52*, 371-375.
57. Yang, J.; Hu, J.; Weng, M.; Tan, R.; Tian, L.; Yang, J.; Amine, J.; Zheng, J.; Chen, H.; Pan, F.,

Fe-Cluster Pushing Electrons to N-Doped Graphitic Layers with $Fe_3C(Fe)$ Hybrid Nanostructure to Enhance O_2 Reduction Catalysis of Zn-Air Batteries. *ACS App. Mater. Interfaces* **2017**, *9*, 4587-4596.

58. Ren, G.; Lu, X.; Li, Y.; Zhu, Y.; Dai, L.; Jiang, L., Porous Core−Shell Fe_3C Embedded N-doped Carbon Nanofibers as an Effective Electrocatalysts for Oxygen Reduction Reaction. *ACS App. Mater. Interfaces* **2016**, *8*, 4118-4125.
59. Song, A.; Cao, L.; Yang, W.; Li, Y.; Qin, X.; Shao, G., Uniform Multilayer Graphene-Coated Iron and Iron-Carbide as Oxygen Reduction Catalyst. *ACS Sustainable Chem. Eng.* **2018**, *6*, 4890-4898.
60. Wu, T.; Zhang, H.; Zhang, X.; Zhang, Y.; Zhao, H.; Wang, G., A low-cost cementite (Fe_3C) nanocrystal@N-doped graphitic carbon electrocatalyst for efficient oxygen reduction. *Phys. Chem. Chem. Phys.* **2015**, *17*, 27527-27533.
61. Yang, Z. K.; Zhao, Z.-W.; Liang, K.; Zhou, X.; Shen, C.-C.; Liu, Y.-N.; Wang, X.; Xu, A.-W., Synthesis of nanoporous structured iron carbide/Fe–N–carbon composites for efficient oxygen reduction reaction in Zn–air batteries. *J. Mater. Chem. A* **2016**, *4*, 19037-19044.
62. Liu, M.; Guo, X.; Hu, L.; Yuan, H.; Wang, G.; Dai, B.; Zhang, L.; Yu, F., Fe_3O_4/Fe_3C@Nitrogen-Doped Carbon for Enhancing Oxygen Reduction Reaction. *ChemNanoMat* **2019**, *5*, 187-193.
63. Lv, M.; Guo, H.; Shen, H.; Wang, J.; Wang, J.; Shimakawa, Y.; Yang, M., Fe_3C cluster-promoted single-atom Fe, N doped carbon for oxygen-reduction reaction. *Phys. Chem. Chem. Phys.* **2020**, *22*, 7218-7223.
64. Zhou, F.; Yu, P.; Sun, F.; Zhang, G.; Liu, X.; Wang, L., The cooperation of Fe_3C nanoparticles with isolated single iron atoms to boost the oxygen reduction reaction for Zn–air batteries. *J.*

Mater. Chem. A **2021**, *9*, 6831-6840.

65. Hu, Y.; Jensen, J. O.; Zhang, W.; Martin, S.; Chenitz, R.; Pan, C.; Xing, W.; Bjerrum, N. J.; Li, Q., Fe_3C-based oxygen reduction catalysts: synthesis, hollow spherical structures and applications in fuel cells. *J. Mater. Chem. A* **2015**, *3*, 1752–1760.
66. Zhong, L.; Frandsen, C.; Mørup, S.; Hu, Y.; Pan, C.; Cleemann, L. N.; Jensen, J. O.; Li, Q., ^{57}Fe-Mössbauer spectroscopy and electrochemical activities of graphitic layer encapsulated iron electrocatalysts for the oxygen reduction reaction. *Appl. Catal. B: Environ.* **2018**, *221*, 406-412.
67. Reda, M.; Hansen, H. A.; Vegge, T., DFT Study of the Oxygen Reduction Reaction on Carbon-Coated Iron and Iron Carbide. *ACS Catal.* **2018**, *8*, 10521-10529.
68. Patniboon, T.; Hansen, H. A., N-Doped Graphene Supported on Metal-Iron Carbide as a Catalyst for the Oxygen Reduction Reaction: Density Functional Theory Study. *ChemSusChem* **2020**, *13*, 996-1005.
69. Sun, T.; Jiang, Y.; Wu, Q.; Du, L.; Zhang, Z.; Yang, L.; Wang, X.; Hu, Z., Is iron nitride or carbide highly active for oxygen reduction reaction in acidic medium? *Catal. Sci. Technol.* **2017**, *7*, 51-55.
70. Tuci, G.; Zafferoni, C.; D'Ambrosio, P.; Caporali, S.; Ceppatelli, M.; Rossin, A.; Tsoufis, T.; Innocenti, M.; Giambastiani, G., Tailoring Carbon Nanotube N-Dopants while Designing Metal-Free Electrocatalysts for the Oxygen Reduction Reaction in Alkaline Medium. *ACS Catal.* **2013**, *3*, 2108-2111.
71. Tuci, G.; Zafferoni, C.; Rossin, A.; Milella, A.; Luconi, L.; Innocenti, M.; Truong Phuoc, L.; Duong-Viet, C.; Pham-Huu, C.; Giambastiani, G., Chemically Functionalized Carbon Nanotubes with Pyridine Groups as Easily Tunable N-Decorated Nanomaterials for the

Oxygen Reduction Reaction in Alkaline Medium. *Chem. Mater.* **2014**, *26*, 3460-3470.

72. Bard, A. J.; Faulkner, L. R., Electrochemical Methods: Fundamentals and Applications. 2nd ed.; John Wiley & Sons, Inc.: New York, 2001; p 856.
73. Wang, Y.; Zhang, D.; Liu, H., A study of the catalysis of cobalt hydroxide towards the oxygen reduction in alkaline media. *J. Power Sources* **2010**, *195*, 3135-3139.
74. Zheng, J.; Yan, Y.; Xu, B., Correcting the Hydrogen Diffusion Limitation in Rotating Disk Electrode Measurements of Hydrogen Evolution Reaction Kinetics. *J. Electrochem. Soc.* **2015**, *162*, F1470–F1481.
75. Murthy, A. P.; Theerthagiri, J.; Madhavan, J., Insights on Tafel Constant in the Analysis of Hydrogen Evolution Reaction. *J. Phys. Chem. C* **2018**, *122*, 23934-23949.
76. Du, C. Y.; Zhao, T. S.; Yang, W. W., Effect of methanol crossover on the cathode behavior of a DMFC: A half-cell investigation. *Electroc. Acta* **2007**, *52*, 5266-5271.
77. Tan, Y. M.; Xu, C. F.; Chen, G. X.; Zheng, N. F.; Xie, Q. J., A Graphene–Platinum Nanoparticles–Ionic Liquid Composite Catalyst for Methanol-Tolerant Oxygen Reduction Reaction. *Energy Environ. Sci.* **2012**, *5*, 6923-6927.
78. Jiang, Y.; Lu, Y.; Wang, X.; Bao, Y.; Chena, W.; Niu, L., A cobalt–Nitrogen Complex on N-Doped Three-Dimensional Graphene Framework as a Highly Efficient Electrocatalyst for Oxygen Reduction Reaction. *Nanoscale* **2014**, *6*, 15066-15072.
79. Kim, D.-W.; Li, O. L.; Saito, N., Enhancement of ORR Catalytic Activity by Multiple Heteroatom-Doped Carbon Materials. *Phys. Chem. Chem. Phys.* **2015**, *17*, 407-413.
80. Briois, V.; Fonda, E.; Belin, S.; Barthe, L.; La Fontaine, C.; Langlois, F.; Ribbens, M.; Villain, F. In *Applications et Développements Récents*, UVX 2010 - 10e Colloque sur les Sources Cohérentes et Incohérentes UV, VUV et X.

81. Ravel, B.; Newville, M., ATHENA, ARTEMIS, HEPHAESTUS: data analysis for X-ray absorption spectroscopy using IFEFFIT. *J. Synchrotron Radiat.* **2005**, *12*, 537-541.

82. Chen, R.; Yang, C.; Cai, W.; Wang, H.-Y.; Miao, J.; Zhang, L.; Chen, S.; Liu, B., Use of Platinum as the Counter Electrode to Study the Activity of Nonprecious Metal Catalysts for the Hydrogen Evolution Reaction. *ACS Energy Lett.* **2017**, *2*, 1070-1075.

TOC graphic

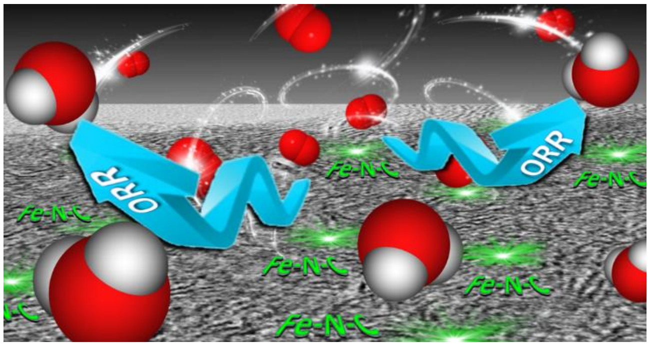

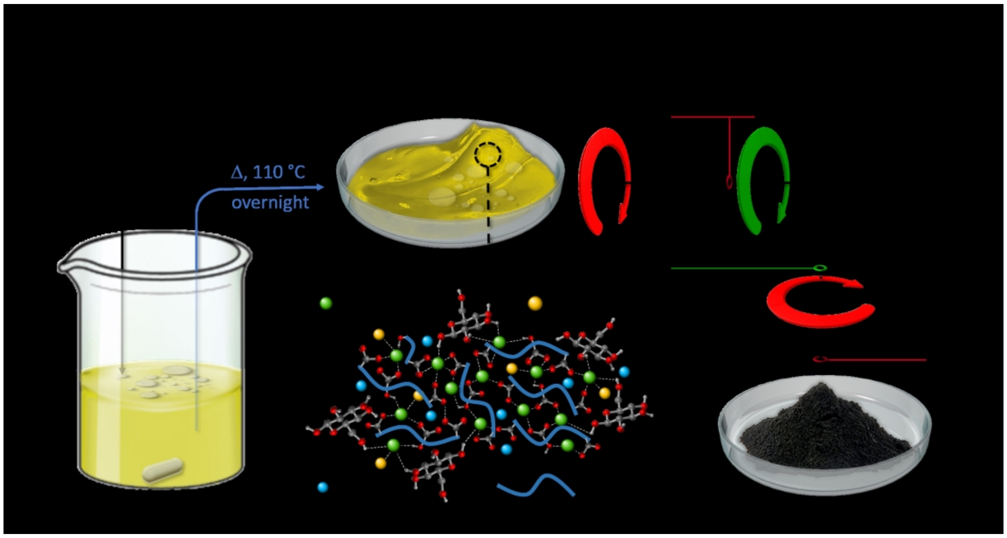

Figure 1

351x186mm (150 x 150 DPI)

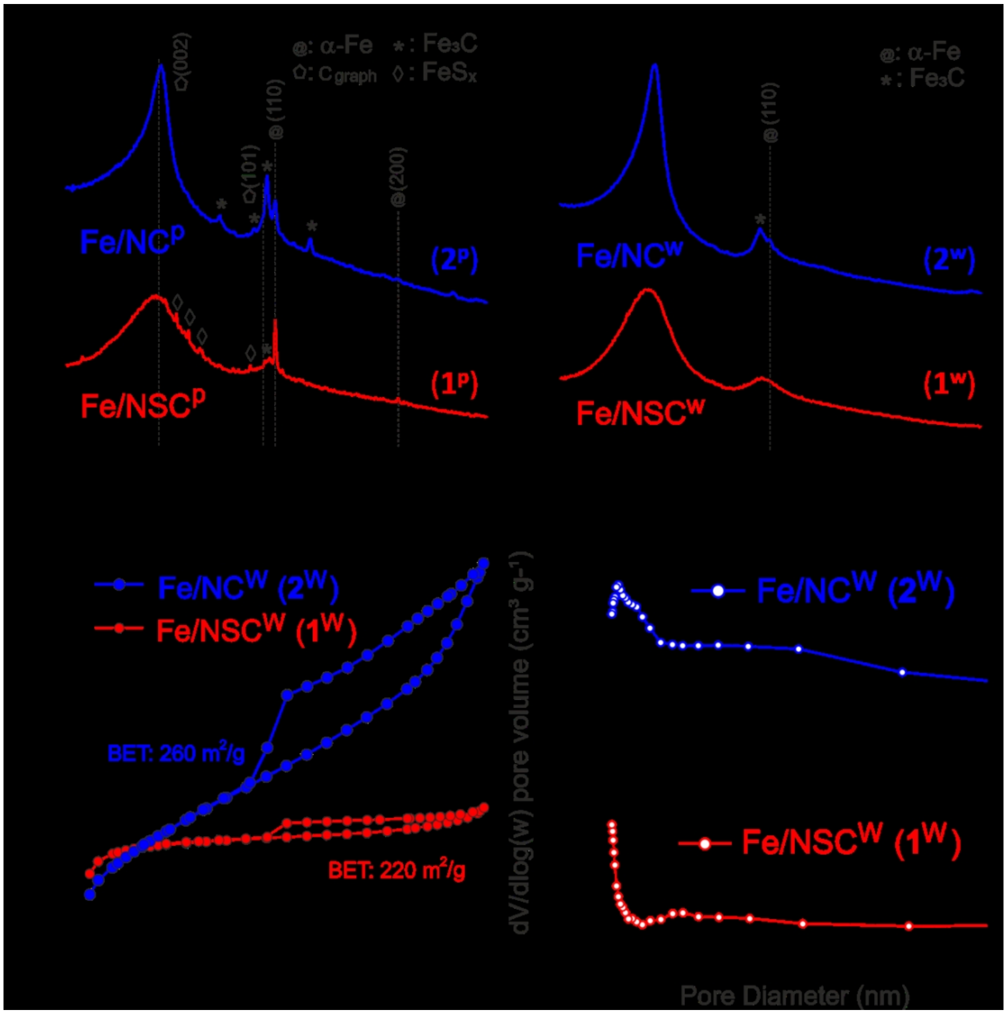

Figure 2

212x213mm (150 x 150 DPI)

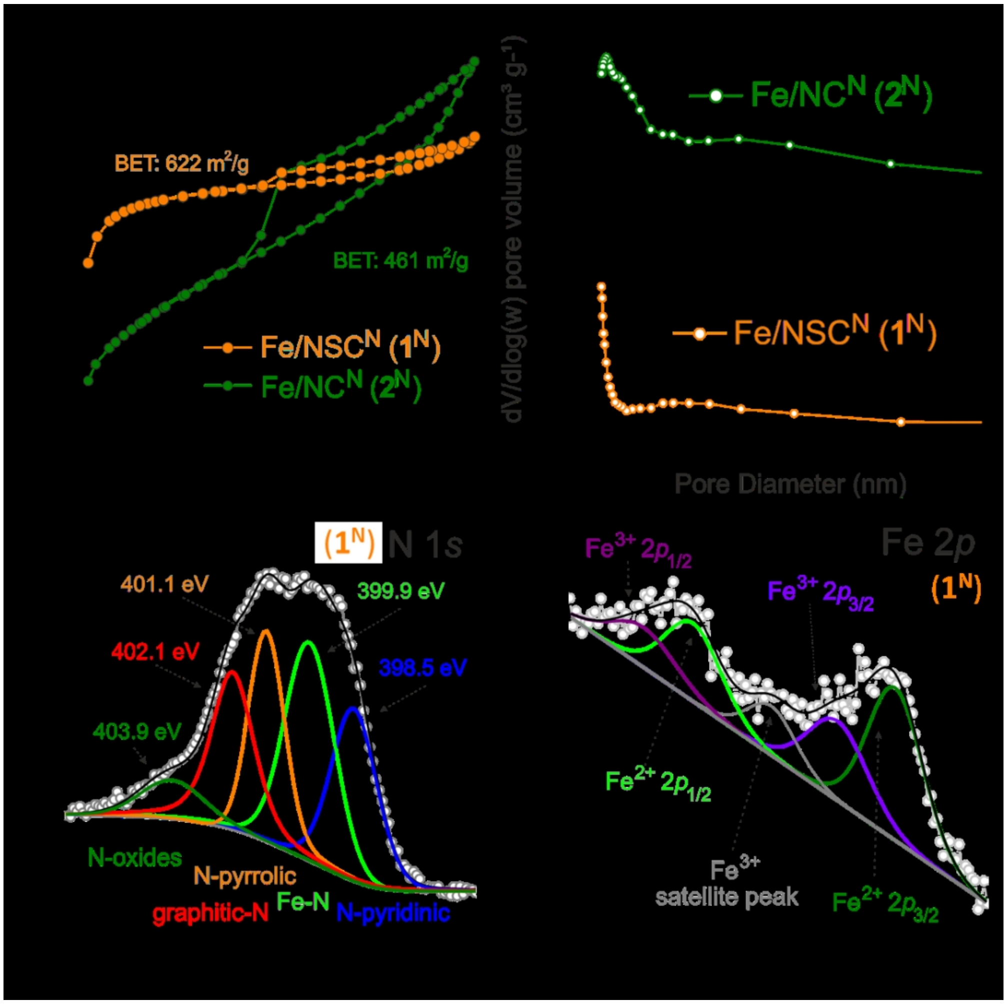

Figure 3

208x207mm (150 x 150 DPI)

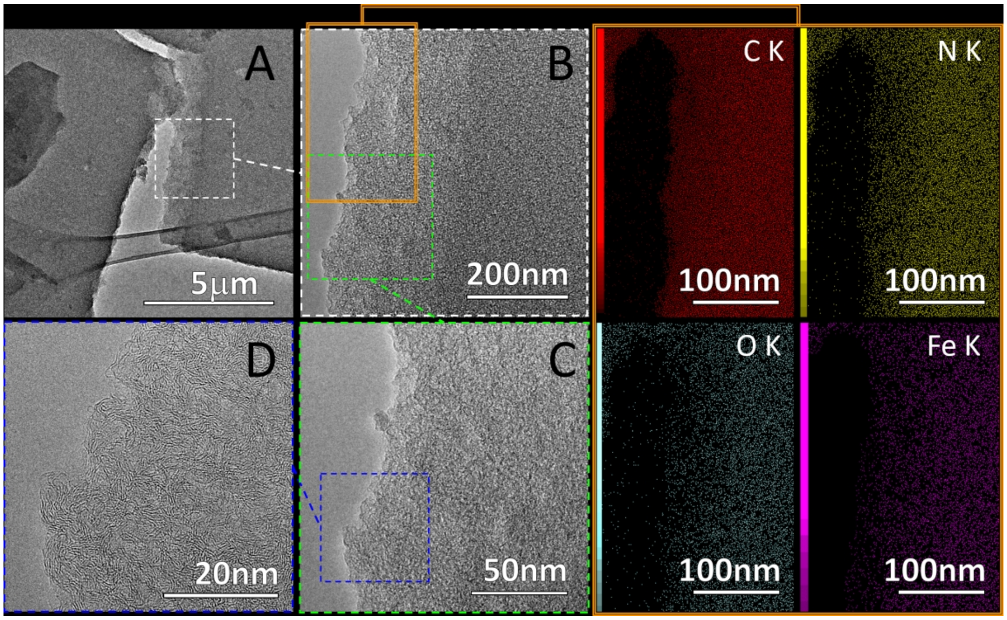

Figure 4

351x215mm (150 x 150 DPI)

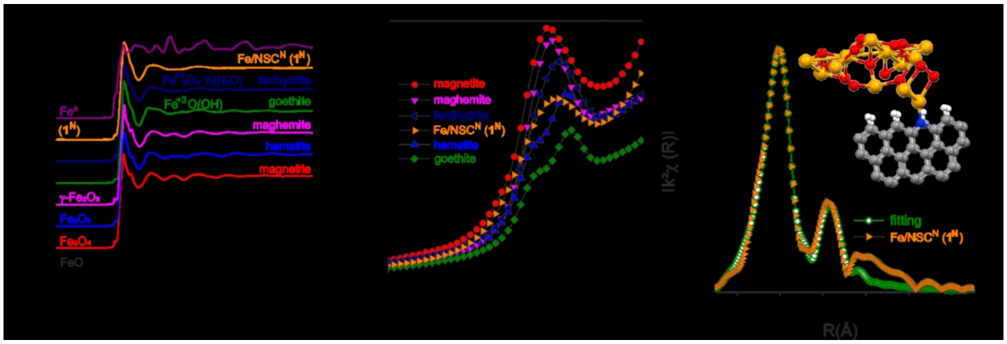

Figure 5

304x102mm (150 x 150 DPI)

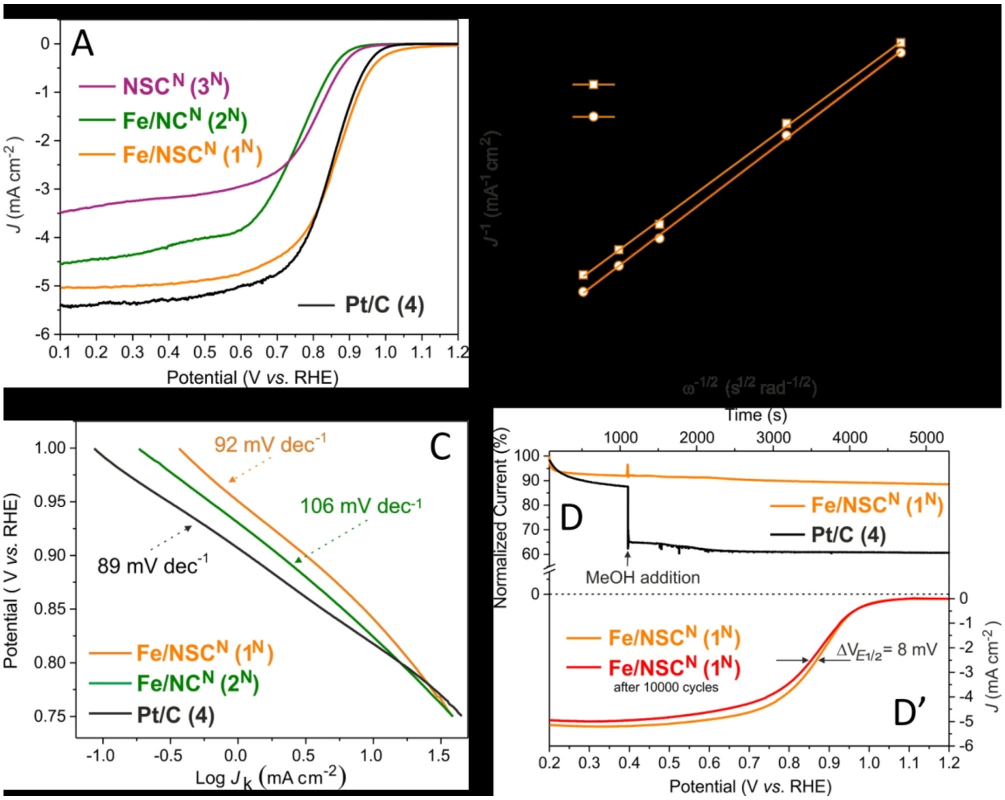

Figure 6

272x215mm (150 x 150 DPI)

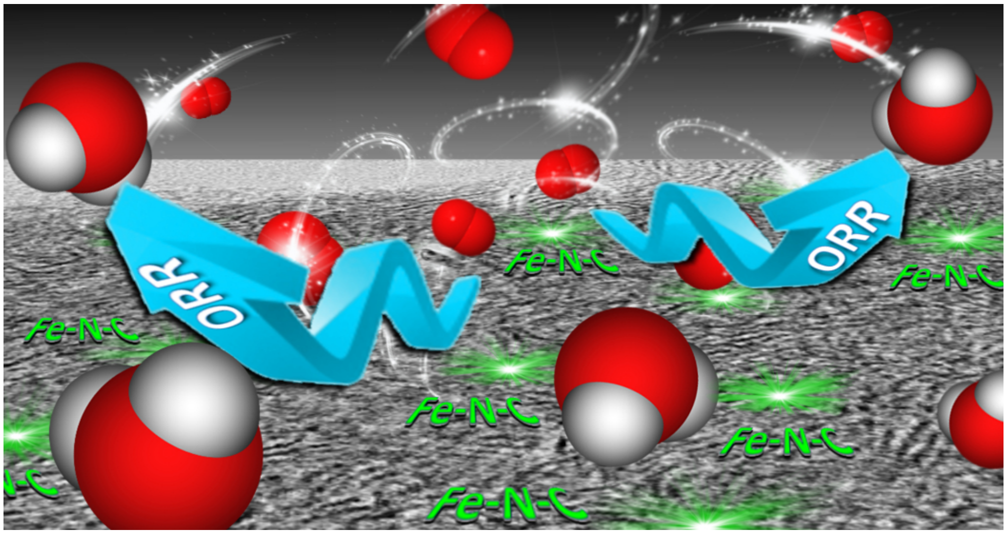

Revised TOC graphic